

THE CARBURIZATION OF TUNGSTEN AND CONVERSION INTO ANISOTROPIC ZIRCONIUM CARBIDE/TUNGSTEN CERMETS

by
Zhenhui Chen

A Thesis

Submitted to the Faculty of Purdue University

In Partial Fulfillment of the Requirements for the degree of

Master of Science in Materials Engineering



School of Materials Engineering

West Lafayette, Indiana

December 2020

THE PURDUE UNIVERSITY GRADUATE SCHOOL
STATEMENT OF COMMITTEE APPROVAL

Dr. Kenneth Sandhage, Chair

School of Materials Engineering

Dr. Kevin Trumble

School of Materials Engineering

Dr. Xinghang Zhang

School of Materials Engineering

Approved by:

Dr. David Bahr

In memorial of Dr. Richard P. Vinci

ACKNOWLEDGMENTS

I would like to thank my advisor, Dr. Kenneth Sandhage, who offered me this great opportunity to work in his group. His passion for work and research really inspired me deeply. I am also truly grateful for his guidance and support through my education and research. I would also like to thank my committee members, Dr. Kevin Trumble Dr. Xinghang Zhang for their guidance and generous supports on my research.

I would also like to acknowledge the support from Dr. Mario Caccia, who gave me precious advice when I was at the hardest time. I would not be able to finish my research without his support and guidance. Additionally, I would like to thank other members in Dr. Sandhage's group, specifically Dr. Saeed Bagherzadeh, Dr. Sunghwan Hwang, Alex, Adam, Liz and others. It was my pleasure to have an opportunity to work with all of them.

Finally, I would like to thank my parents. I would not be able to make this far without their continuous love and support.

TABLE OF CONTENTS

LIST OF TABLES	6
LIST OF FIGURES	7
1. ABSTRACT	11
2. INTRODUCTION	12
2.1 Possible Carburization Rate Laws	20
2.1.1 Linear Rate Law	20
2.1.2 Parabolic Rate Law	20
2.1.3 Cubic Rate Law	21
2.1.4 Paralinear Rate Law	21
3. EXPERIMENTAL PROCEDURES	22
3.1 Reaction of W plates with pure CO gas	22
3.2 Characterization of the carburized layer	23
3.3 Inert marker experiment	24
3.4 Preparation and Sintering of a Tungsten Wire Preform	24
3.5 Carburization of Sintered Tungsten Wire	25
3.6 Preparation of the Zr_2Cu alloy	25
3.7 Infiltration of Tungsten Wire Sample	26
3.8 Characterization of Tungsten Wire Sample	26
4. RESULTS AND DISCUSSION	27
4.1 Kinetic Mechanism of Tungsten Carburization with CO Gas	27
4.2 Fabrication of Anisotropic ZrC/W Composites	53
5. CONCLUSIONS	59
REFERENCES	60

LIST OF TABLES

Table 1. Polishing procedure for pure tungsten plate samples.	22
Table 2. Surface roughness of the large face of the unreacted W plate and reacted with CO gas at 1000 °C for 12 h, 48 h, and 96 h.	35
Table 3. Calculated ΔG° values for Rxn. (R2) and (R3) at 1200 K, 1273 K, and 1300 K.	37
Table 4. The equilibrium partial pressure P_{CO_2}/P_{CO} for Rxn. (R2) and (R3) at 1273 K.	38
Table 5. ΔG values for Rxn. (R2) and (R3) at 1273 K.	38
Table 6. Mass change per area versus reaction time data for W plates reacted with pure CO gas at 1000 °C for 12 to 96 h.	39
Table 7. Thickness of the WC film versus reaction time data for W plates reacted with pure CO gas at 1000 °C for 12 to 96 h.	42
Table 8. Calculated crystallite size of the WC film using Williamson-Hall analysis for W plates reacted with pure CO gas at 1000 °C for 12 to 96 h.	48

LIST OF FIGURES

Figure 1. Schematic illustrations of the WC preform converting to ZrC/W via the DCP process, where (a) shows the WC preform infiltrated with Zr-bearing melt, (b) shows the partial reaction between WC and Zr in the melt, and (c) shows the complete reaction between WC and Zr in the melt.	13
Figure 2. Photographs of (a) a ZrC/W rocket nozzle [8] and (b) a dense ZrC/W heat exchanger plate [9].	13
Figure 3. BSE image of the ZrC/W composite fabricated by reactive infiltration of Zr_2Cu into porous WC preform.	14
Figure 4. SEM images of the ZrC/W composites fabricated using the DCP process with a porous WC preform containing 20 vol% WC fibers. (a) and (b) are the cross section parallel to the pressing direction, (c) and (d) are perpendicular to the press direction [17].	15
Figure 5. Schematic illustrations of each step for fabricating anisotropic ZrC/W composites from the tungsten wire preform, where (a) shows tungsten wires winding on a MgO/Mo spool, (b) shows sectioning of the rigid sample from the spool after sintering and partial carburization to WC, and (c) shows the partial carburized W wire preform converting to the ZrC/W composite via the DCP method.....	17
Figure 6. Schematic illustrations of different stages for metal wires during sintering, where (a) is before sintering, (b) is the intermediate sintering stage, and (c) is the final spheroidization stage [18]......	17
Figure 7. Photographs of (a) 20 μm diameter tungsten wire wound on a molybdenum spool, and (b) the rectangular sample section from the spool after sintering [19].	18
Figure 8. SEM image of a cross section of wound tungsten wire with 20 μm diameter after sintering at 2075 $^{\circ}C$ for 75 min [19].	18
Figure 9. Photographs of the setup for W plate exposure to CO gas: (a) top view and (b) side view.	22
Figure 10. Photographs of (a) the assembly for winding the W wire on a MgO plate, and (b) the W wire wound on the MgO plate.	25
Figure 11. Schematic illustration of the setup for tungsten wire preform infiltration.	26
Figure 12. SE images of the polished surface of the pure tungsten plate at (a) a lower magnification and (b) a higher magnification and associated elemental map of (c) tungsten, and (d) the EDX spectrum.	27
Figure 13. XRD pattern obtained from the polished surface of the unreacted tungsten plate.....	28
Figure 14. AFM image (25 μm x 25 μm) of the surface roughness of the pure W plate.....	28

Figure 15. SE images of the polished surface of the pure tungsten plate at (a) a lower magnification and (b) a higher magnification and associated elemental maps of (c) carbon and (d) tungsten after reaction with pure CO gas at 1000 °C for 12 h, and (e) the EDX spectrum.	29
Figure 16. SE images of the polished surface of the pure tungsten plate at (a) a lower magnification and (b) a higher magnification and associated elemental maps for (c) carbon and (d) tungsten after reaction with pure CO gas at 1000 °C for 24 h, and (e) the EDX spectrum.	30
Figure 17. SE images of the polished surface of the pure tungsten plate at (a) a lower magnification and (b) a higher magnification and associated elemental maps for (c) carbon and (d) tungsten after reaction with pure CO gas at 1000 °C for 36 h, and (e) the EDX spectrum.	31
Figure 18. SE images of the polished surface of the pure tungsten plate at (a) a lower magnification and (b) a higher magnification and associated elemental maps for (c) carbon and (d) tungsten after reaction with pure CO gas at 1000 °C for 48 h, and (e) the EDX spectrum.	32
Figure 19. SE images of the polished surface of the pure tungsten plate at (a) a lower magnification and (b) a higher magnification and associated elemental maps for (c) carbon and (d) tungsten after reaction with pure CO gas at 1000 °C for 96 h, and (e) the EDX spectrum.	33
Figure 20. XRD patterns obtained from surfaces of W plates after reaction with pure CO gas at 1000 °C for 12 to 96 h.	34
Figure 21. AFM images (25 µm x 25 µm) of the surface roughness of W plates after reaction with pure CO gas at 1000 °C for (a) 12 h, (b) 48 h, and (c) 96 h.	35
Figure 22. (a) STEM image of the ion-milled cross-section of the tungsten plate after reaction with pure CO gas at 1000 °C for 12 h showing a WC layer and W substrate, and the SAED pattern from (b) the tungsten substrate with a zone axis of [001] and from (c) the WC layer with a zone axis of [110] (Courtesy of Bo Yang)	36
Figure 23. Plot of the mass change per area versus reaction time for W plates after reaction with pure CO gas at 1000 °C for 12 to 96 h.	40
Figure 24. Plot of the log (mass change per area) versus log (reaction time) for W plates after reaction with pure CO gas at 1000 °C for 12 to 96 h.	40
Figure 25. Plot of the mass change per area versus time ^{1/2} for W plates after reaction with pure CO gas at 1000 °C for 12 to 96 h.	41
Figure 26. Plot of the mass change per area versus time ^{1/3} for W plates after reaction with pure CO gas at 1000 °C for 12 to 96 h.	41
Figure 27. SEM image of the FIB-cut cross-section of the W plate after reaction with pure CO gas at 1000 °C for 24 h. The thickness of the film was determined by measuring at 15 different locations as labeled in the image above. (FIB cut was operated by Dr. Sunghwan Hwang)	42
Figure 28. High resolution SE images of the FIB-cut cross-section of the W plate reacted with pure CO gas at 1000 °C for 12 h. (FIB cut was operated by Dr. Sunghwan Hwang).....	43
Figure 29. High resolution SE images of the FIB-cut cross-section of the W plate reacted with pure CO gas at 1000 °C for 24 h. (FIB cut was operated by Dr. Sunghwan Hwang).....	43

Figure 30. High resolution SE images of the FIB-cut cross-section of the W plate reacted with pure CO gas at 1000 °C for 36 h. (FIB cut was operated by Dr. Sunghwan Hwang).....	44
Figure 31. High resolution SE images of the FIB-cut cross-section of the W plate reacted with pure CO gas at 1000 °C for 48 h. (FIB cut was operated by Dr. Sunghwan Hwang).....	44
Figure 32. High resolution SE images of the FIB-cut cross-section the W plate reacted with pure CO gas at 1000 °C for 96 h. (FIB cut was operated by Sunghwan Hwang).....	45
Figure 33. Plot of the WC film thickness versus reaction time for W plates after reaction with pure CO gas at 1000 °C for 12 to 96 h.	46
Figure 34. Plot of the log (WC film thickness) versus log (reaction time) for W plates after reaction with pure CO gas at 1000 °C for 12 to 96 h.	46
Figure 35. Plot of the WC film thickness versus reaction time ^{1/2} for W plates after reaction with pure CO gas at 1000 °C for 12 to 96 h.	47
Figure 36. Plot of the WC film thickness versus time ^{1/3} for W plates after reaction with pure CO gas at 1000 °C for 12 to 96 h.	47
Figure 37. TEM images of the tungsten plate reacted with pure CO gas at 1000 °C for 12 h.	49
Figure 38. TEM images of the tungsten plate reacted with pure CO gas at 1000 °C for 96 h.	49
Figure 39. (a) SE image of the large face of the tungsten plate containing MgO particles (inert markers) before the reaction. EDX elemental maps of (b) tungsten, (c) magnesium, and (d) oxygen.	50
Figure 40. (a) SE image of the large face of the W plate containing MgO particles (inert markers) after the reaction with CO gas at 1000 °C for 96 h. EDX elemental maps of (b) carbon, (c) magnesium, (d) oxygen, and (e) tungsten.	51
Figure 41. (a) SE image and EDX elemental maps of (b) platinum, (c) magnesium, (d) oxygen, (e) carbon, and (f) tungsten obtained from the FIB-cut cross-section of the tungsten plate containing MgO particles (inert markers) after reaction with CO gas at 1000 °C for 96 h.	52
Figure 42. Photograph of the sectioned rectangular W wire preform after sintering at 1800 °C for 2 h with flowing of ultra-high purity argon (99.999%).	53
Figure 43. SEM images of the W wire preform sintered at 1800 °C for 2 h with flowing ultra-high purity argon (99.999%) from (a) tilted cross-sectional view and (b) side view.	53
Figure 44. XRD pattern obtained from the surface of the W wire preform sintered at 1800 °C for 2 h with flowing of ultra-high purity argon (99.999%).	54
Figure 45. XRD pattern obtained from the surface of the W wire preform after reaction with pure CO gas at 1000 °C for 96 h.	54
Figure 46. XRD pattern obtained from the surface of the W wire sample reactively infiltrated with Zr ₂ Cu at 1350 °C.	56

Figure 47. BSE images from a cross-sectional view of the reactive infiltrated carburized W wire preform at (a) a high magnification and (b) a lower magnification and associated elemental maps of (c) tungsten, (d) zirconium, (e) carbon, (f) copper, and (g) oxygen. 57

Figure 48. BSE images from a side view of the reactive infiltrated carburized W wire preform at (a) a high magnification and (b) a lower magnification and associated elemental maps of (c) tungsten, (d) zirconium, (e) carbon, (f) copper, and (g) oxygen. 58

1. ABSTRACT

Anisotropic ceramic/metal composites can be attractive due to their tailorable and directional thermal and mechanical properties. As one of the ceramic/metal composites, ZrC/W composites fabricated by the reactive infiltration method, known as the Displacive Compensation of Porosity (DCP) method, have been found to exhibit impressive thermal and mechanical properties. Here, we proposed a novel method for fabricating anisotropic ZrC/W composites via the DCP method from wound tungsten wire preforms. Tungsten wire is wound and sintered to form a rigid preform. The preform is carburized with CO gas to form WC and then converted to ZrC/W with Zr₂Cu liquid via the DCP method. The kinetic mechanism of the formation of WC for the reaction between W and CO gas at 1000 °C was investigated by carburizing W plates with CO gas for 12 h, 24 h, 36 h, 48 h, and 96 h. Thickening rates of the WC films have been found to follow the parabolic rate law, which indicated that the formation of WC film with CO gas was limited by the lattice diffusion of reactant species through the WC film. An inert marker experiment reveals that the formation of WC with the reaction between W and CO gas was controlled by the inward diffusion of C through the WC film. The feasibility of fabricating anisotropic ZrC/W composites via the DCP method from the wound tungsten wire preform was validated. A rigid tungsten wire preform was prepared by hand-winding and sintering at 1800 °C. The preform was carburized with CO gas at 1000 °C for 96 h. XRD analyses confirmed the formation of WC coated W. An anisotropic ZrC/W composite was successfully fabricated by infiltrating the carburized preform with Zr₂Cu liquid. XRD and EDX analyses confirmed the conversion of WC to ZrC/W.

2. INTRODUCTION

Metal/ceramic composites, especially those comprised of a refractory metal matrix and carbides, are among the most promising materials for high temperature applications due to their excellent mechanical properties, including high fracture toughness and high resistance to creep, erosion, and thermal shock [1] – [4]. ZrC/W composites are a good example of such materials. Zirconium carbide (ZrC) and tungsten (W) are chemically compatible with limited mutual solid solubility [5]. Both zirconium carbide (ZrC) and tungsten (W) are refractory materials with high melting temperatures (up to 3445 °C for ZrC and 3422 °C for W) [6][7]. Additionally, ZrC/W composites have been found to be highly resistant to thermal shock [8]. A ZrC/W rocket nozzle survived a Pi-K test, in which the nozzle was rapidly heated to about 3245 K in 4.6 s [8]. These composites possess high failure strength and creep resistance at high temperatures [9]. Hot isostatic pressing (HIP) is a common method for fabricating ZrC/W composites [10]. However, this process is slow, requires high temperatures and pressures (e.g., using an applied stress of 20 MPa at 2000 °C for 1 h for ZrC/W), and is capable of generating only a limiting range of geometries [10].

The Displacive Compensation of Porosity (DCP) method is a novel process to produce complex and near net-shape metal/ceramic composites via displacement reactions between molten metals and solid ceramics [11]. The process involves pressureless infiltration of molten metals into porous ceramic preforms. The reactions are required to have ceramic and metal products that have a combined larger molar volume than the starting reactant ceramic for self-densification of the preform [12]. A schematic illustration of the DCP method is shown in Figure 1. In the case of ZrC/W, the melt used is a Zr-bearing melt, which is infiltrated into pores of a WC preform. The displacement reaction between WC and Zr yields W and ZrC on the outside of WC particles. Once the reaction is completed, all WC particles are consumed and converted to W and ZrC. Since the combined molar volume of ZrC and W is approximately twice the molar volume of WC ($V_m [\text{ZrC} + \text{W}] = 2.01V_m [\text{WC}]$) [8], if the preform is about 50% porous, then pores will be filled by the reaction to yield a fully dense composite. The shape of the preform can be preserved after reaction (the DCP method is also a near net-shape process). For fabricating ZrC/W composites, WC powders are typically cold-pressed and sintered to form rigid porous preforms [8]. The porous tungsten carbide (WC) preform is then immersed into a Zr_2Cu melt at 1150 °C. At last, the preform is removed from the melt and heated to 1300 °C to finalize the following displacement reaction:



The whole process is pressureless and requires much lower temperatures compare to the HIP method. ZrC/W composites fabricated via the DCP method have been used in devices such as heat exchangers and rocket nozzles [9] as shown in Figure 2. Figure 3 shows the isotropic structure of the ZrC/W heat exchanger fabricated by the DCP method [9]. Co-continuous W-bearing phases (bright phases including W and residual WC) are uniformly distributed along with ZrC (dark phase).

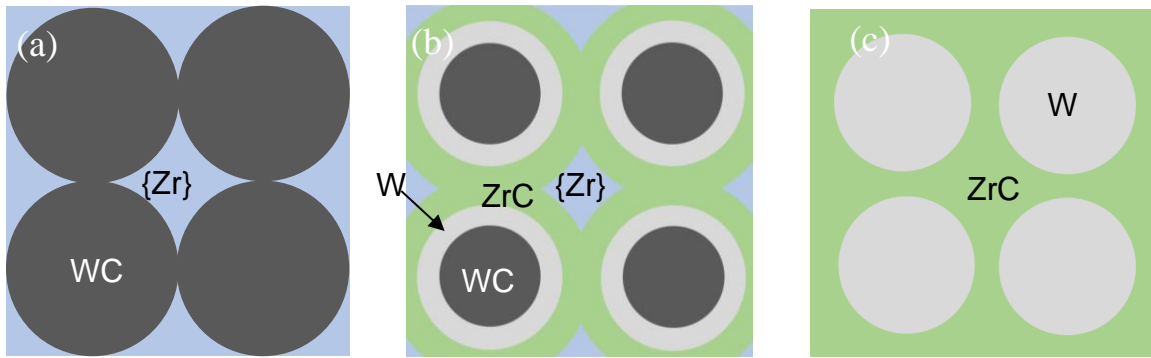


Figure 1. Schematic illustrations of the WC preform converting to ZrC/W via the DCP process, where (a) shows the WC preform infiltrated with Zr-bearing melt, (b) shows the partial reaction between WC and Zr in the melt, and (c) shows the complete reaction between WC and Zr in the melt.

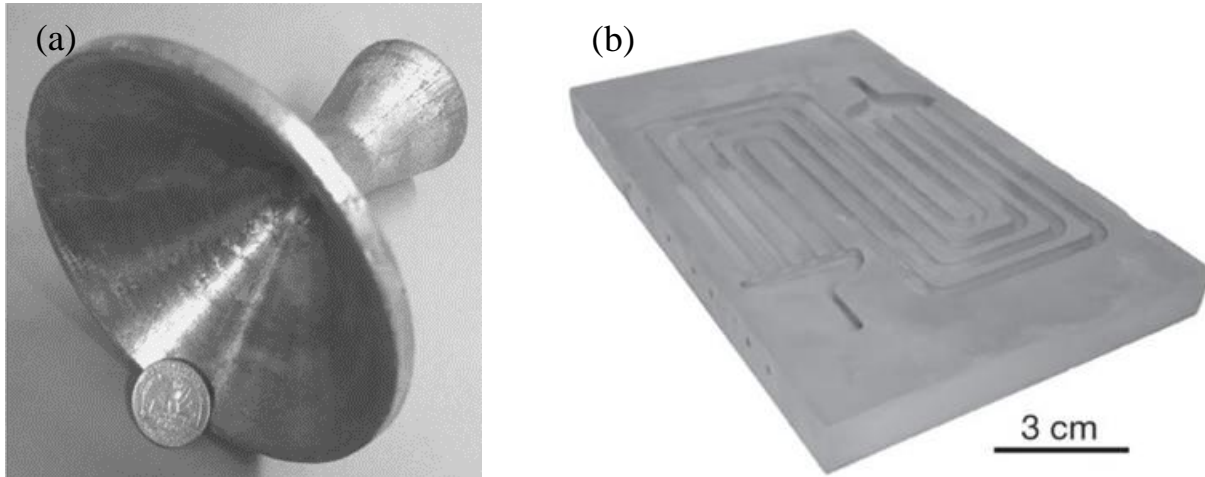


Figure 2. Photographs of (a) a ZrC/W rocket nozzle [8] and (b) a dense ZrC/W heat exchanger plate [9].

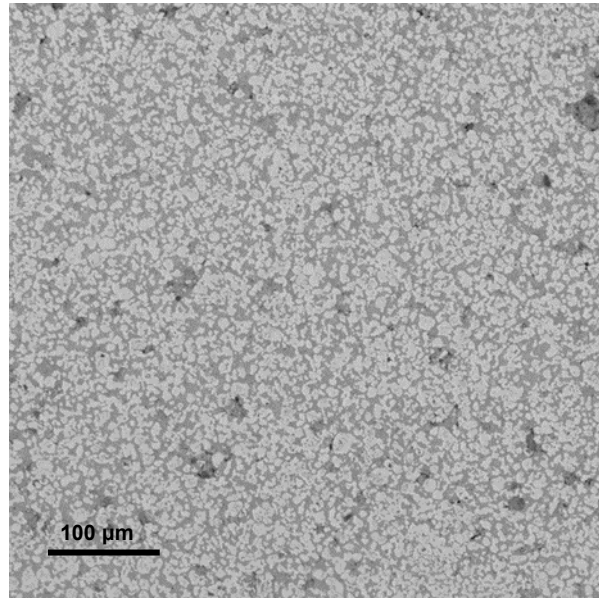


Figure 3. BSE image of the ZrC/W composite fabricated by reactive infiltration of Zr_2Cu into porous WC preform.

Mechanical and thermal behavior of ZrC/W composites fabricated via the DCP process described exhibit isotropic behavior consistent with their isotropic microstructure [13]. However, some applications can require the materials to possess anisotropic thermal or mechanical properties, such as for heat exchangers and certain aerospace components. Furthermore, some researchers have found that the anisotropic microstructure of metal/ceramic composites can cause significant thermophysical anisotropy. For example, a directional SiC/Cu-Si composite has exhibited both a higher thermal conductivity and a lower coefficient of thermal expansion in the longitudinal direction [14]. The preform for this composite was prepared by the infiltration of molten Cu-Si alloy into a SiC preform with directional pores. Roy et al. [15] also reported that directional $\text{Al}_2\text{O}_3/\text{Al}$ composites, fabricated by freeze-casting, exhibited a lower CTE value along the longitudinal direction. Continuous metal fibers can also act to toughen the composite due to a crack bridging mechanism. Under the loading condition, the separation of metal/ceramic interface consumes energy, and can relax the stress at the crack tip. Continuous metal fibers can establish a more significant bridging effect, which further helps to toughen the composite in the transverse direction [16]. Therefore, ZrC/W composites with anisotropic structure and their thermal and mechanical properties would be interesting to study.

The fabrication of ZrC/W composites with certain control of phase contiguity using the DCP method had been studied by Lipke [17]. Carbon fibers and graphitic foams were first converted into WC/W fibers via the reaction with tungsten oxychloride. WC/W fibers were then mixed with WC powders and pressed into a rigid preform. At last, the preform was converted into a ZrC/W composite via the DCP process by infiltration with a Zr_2Cu melt and reaction at 1300 °C for 4 h. The microstructure of the resulting composite exhibited limited anisotropy, as shown in Figure 4 .

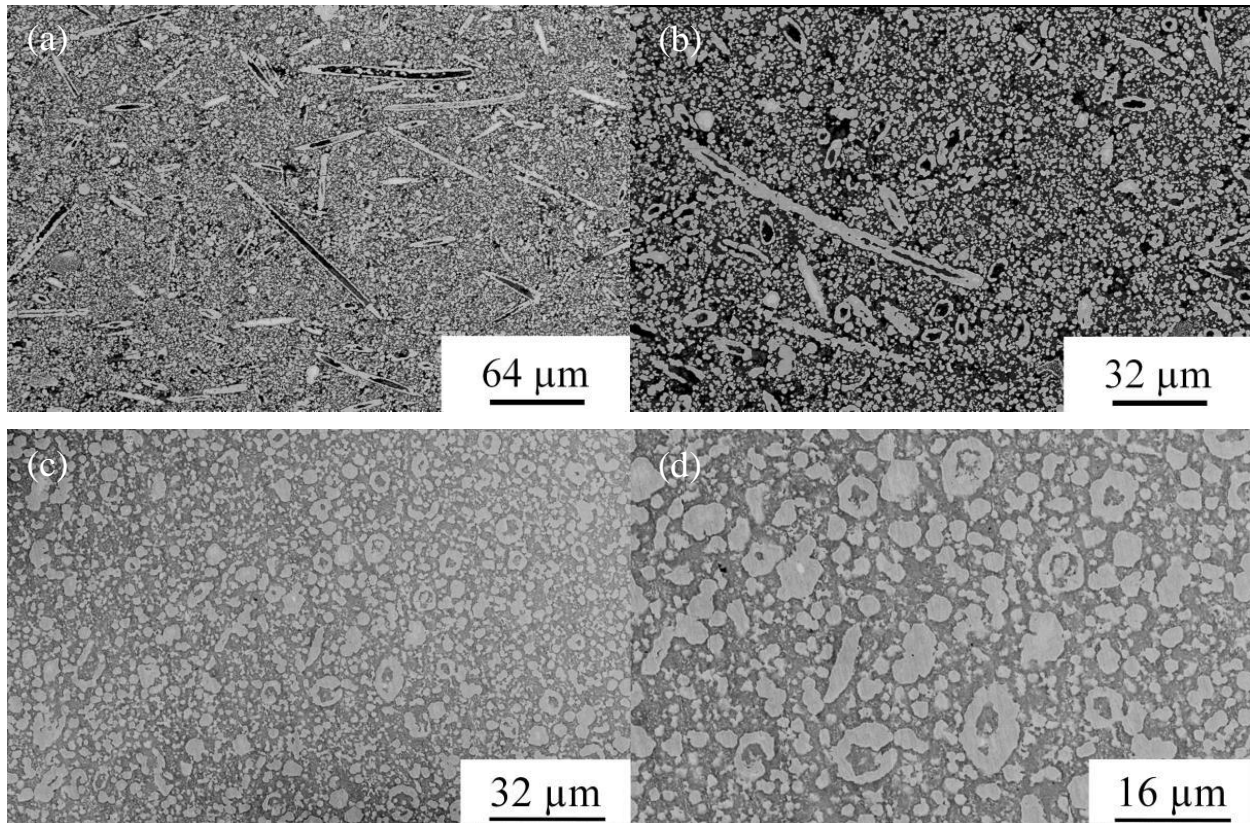


Figure 4. SEM images of the ZrC/W composites fabricated using the DCP process with a porous WC preform containing 20 vol% WC fibers. (a) and (b) are the cross section parallel to the pressing direction, (c) and (d) are perpendicular to the press direction [17].

A new method utilizing the DPC process to produce highly anisotropic ZrC/W composites is proposed in this thesis. ZrC/W composites produced by the DCP method have utilized cold pressing of WC/binder powder mixtures for preform fabrication. The final microstructure of the composites is affected by the structure of the porous WC preform. The cold pressing method tends to produce WC preforms with a relatively uniform porous structure. The new method proposed here is using tungsten wire to fabricate the shaped preform by winding wires on a MgO spool. The wound tungsten wire preform is then sintered to become rigid (necking between adjacent wires), and then carburized to tungsten carbide. Finally, the carburized tungsten wire preform is converted to ZrC/W composite with a highly anisotropic structure via the DCP method. Figure 5 shows the schematic illustration for each step of this new method. Tungsten wire is commercially available, and the diameter of the available wire ranges from 10 μm to 250 μm . By winding the tungsten wire on a rectangular spool, rectangular tungsten plates can be produced. The pores between wires are highly anisotropic. Pore shape and size are determined by the sintering temperature and time as well as the packing of the wire during winding. Figure 6 shows three stages for the sintering of metal wires [18]. Figure 6(a) shows the void shape before sintering. Figure 6 (b) is the intermediate stage of sintering. Continuing the diffusion, the pores in the final stage shown in Figure 6(c) are spheroidized. In general, the pore size of wound wires keeps shrinking as the sintering continues. Determining the relationship between the pore size and the sintering temperature and time for different size wires allows for the control of the porosity of the final preform. Ives et al. [19] have performed a preliminary sintering experiment on wound tungsten wires. Tungsten wires with 20 μm diameter were wound on a rectangular molybdenum spool as shown in Figure 7a. Figure 7b shows a bulk section of the wound tungsten wire sectioned from the side of the whole sample. The sample was sintered at 2075 $^{\circ}\text{C}$ for 75 mins. The SEM image of the cross-section in Figure 8 shows an intermediate stage of sintering. Additional experiments are required to determine the relationship between sintering conditions and the pore size for different size tungsten wire diameters to precisely control the porosity of the preform.

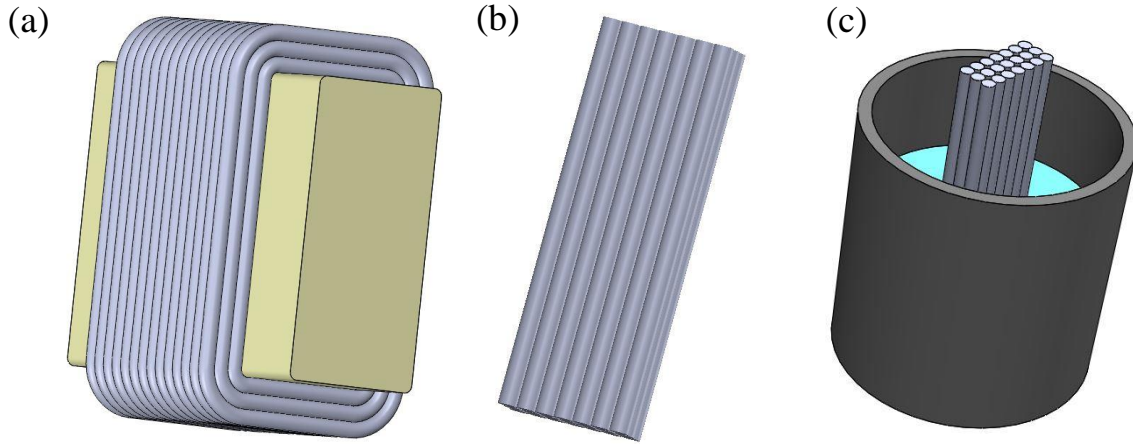


Figure 5. Schematic illustrations of each step for fabricating anisotropic ZrC/W composites from the tungsten wire preform, where (a) shows tungsten wires winding on a MgO/Mo spool, (b) shows sectioning of the rigid sample from the spool after sintering and partial carburization to WC, and (c) shows the partial carburized W wire preform converting to the ZrC/W composite via the DCP method.

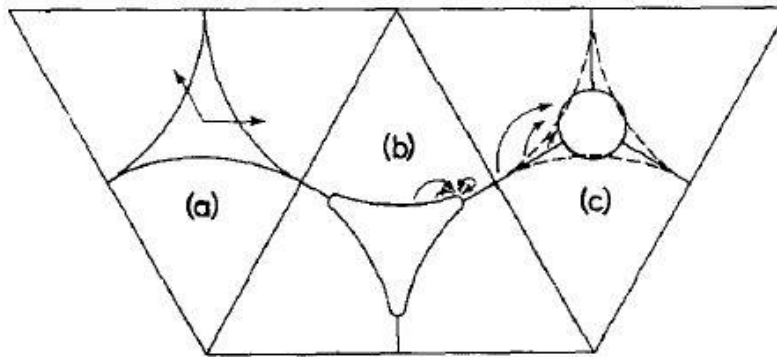


Figure 6. Schematic illustrations of different stages for metal wires during sintering, where (a) is before sintering, (b) is the intermediate sintering stage, and (c) is the final spheroidization stage [18]

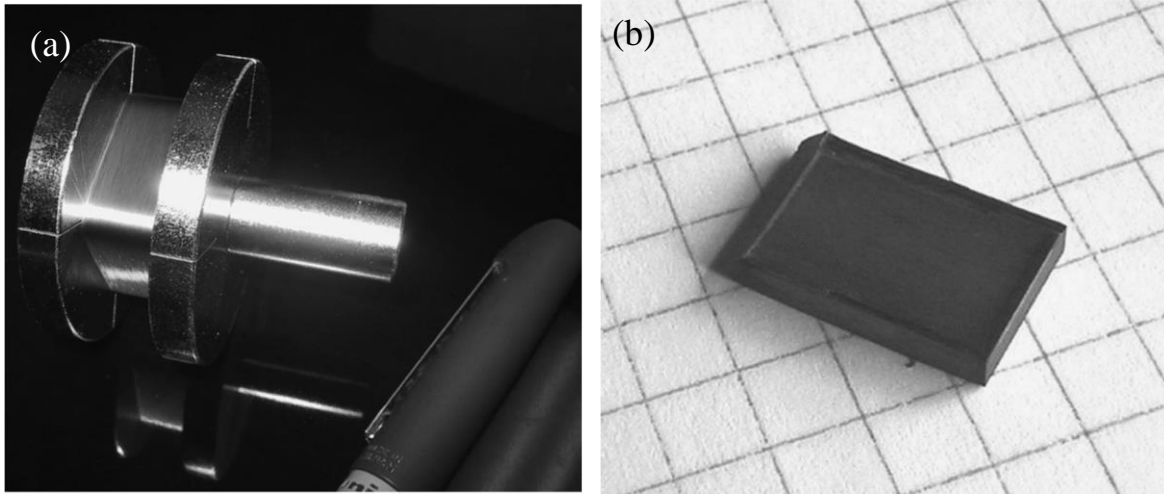


Figure 7. Photographs of (a) 20 μm diameter tungsten wire wound on a molybdenum spool, and (b) the rectangular sample section from the spool after sintering [19].

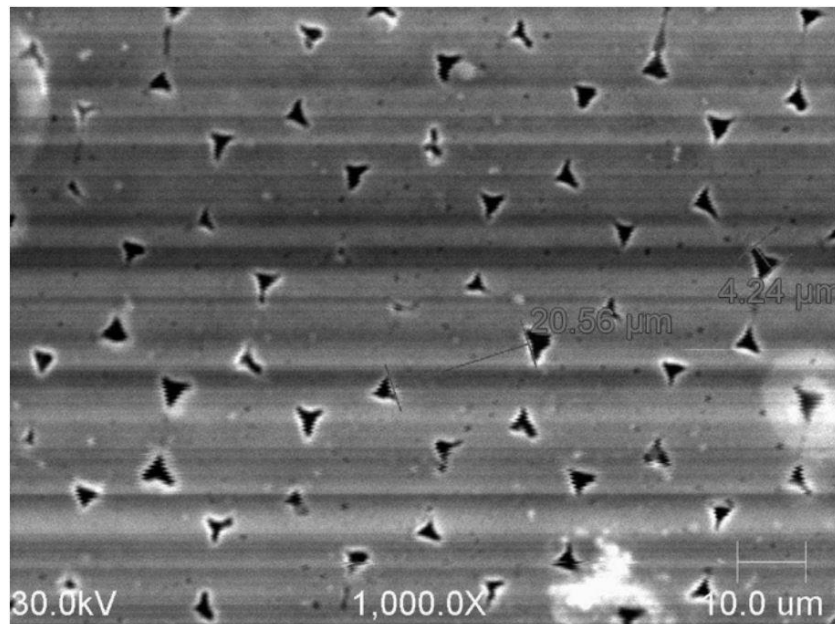


Figure 8. SEM image of a cross section of wound tungsten wire with 20 μm diameter after sintering at 2075 $^{\circ}\text{C}$ for 75 min [19]

A crucial step for this novel preform fabrication process is the carburization of pure tungsten to tungsten carbide. Current processes for tungsten carburization can be divided into two categories: i) carburization with a solid carbon source, where the pure tungsten is in physical contact with a solid carbon source; and ii) carburization with a gaseous carbon source, where the pure tungsten is reacted with a C-bearing vapor species. Carburization with a solid carbon source requires high temperatures (1400 – 1600 °C) under the flow of hydrogen [20]. Hydrogen is used to create a favored partial pressure of P_{CH_4}/P_{H_2} to transport C for the reaction. In addition, applying a carbon source into the pores for the wound tungsten wire preform would be challenging. Carburization with a gaseous carbon source can occur at a relatively low temperature (750 – 1100 °C) [20] [21]. C-bearing gases could enter the pores of a wound tungsten preform and carburize the whole sample. A methane – hydrogen mixture is a popular choice for tungsten carburization [20] [22] [23]. However, this mixture requires a high percentage of hydrogen, which typically is 90 % [20]. A high concentration of hydrogen exposure can result in the embrittlement of tungsten, which may affect the mechanical properties of the final composites [24]. To avoid the embrittlement of the sample, carbon monoxide was chosen in this work as an alternate C-bearing gas. The carburization occurs in a range of temperatures as low as 700 to 900 °C for CO gas [21].

In order to control the carburization rate of the wound tungsten wire for continuous composite fabrication, the rate of reaction of CO with pure tungsten needs to be understood. The kinetics of tungsten carburization using methane-hydrogen mixtures has been studied [22], but no reports were found for kinetics of W carburization using CO gas. The purpose of the present thesis is to determine the kinetic mechanism, including the rate-limiting step and associated rate law, for the carburization of W into WC via reaction with CO gas. The feasibility of fabricating anisotropic ZrC/W composites via the DCP method from the wound carburized tungsten wire preform will also be validated in this thesis.

2.1 Possible Carburization Rate Laws

2.1.1 Linear Rate Law

A linear rate is independent of time, which can be expressed by the following equations:

$$\Delta x = kt + C \quad \text{or} \quad \Delta m/A = k_g t + C' \quad (\text{E1})$$

where k and k_g are linear rate constants for thickness and mass change per unit area respectively, Δx is the carbide film thickness, $\Delta m/A$ is the mass change per unit area, t is the carburization time and C and C' are constants. A linear carburization rate can occur if one of the following steps is limiting the overall rate of carburization:

- Diffusion of a reactant or product gas species through a gaseous boundary layer of constant thickness with time [25]
- Chemical reaction at the gas/carbide or carbide/metal interface [26]
- Solid state diffusion through a dense, continuous carbide layer of constant thickness under a thickening porous carbide scale [27]

2.1.2 Parabolic Rate Law

The parabolic rate law for oxidation was first derived by Tammann, and by Pilling and Bedworth [28] [29] and can also be applied to other gas-solid reactions like carburization. In this case, the carbide layer is assumed to be flat, uniform, and dense. The thickening rate of the carbide scale is proportional to the flux of reactant species across the reaction zone which is inversely proportional to the scale thickness [30]. The expression of the parabolic rate law can be written as

$$\Delta x = (2kt)^{1/2} + C \quad \text{or} \quad \Delta m/A = (k_g t)^{1/2} + C' \quad (\text{E2})$$

where k and k_g are parabolic rate constants for thickness and mass change per unit area respectively, Δx is the carbide film thickness, $\Delta m/A$ is the mass change per unit area, t is the carburization time and C and C' are constants. A parabolic carburization rate can occur if one of the following steps is limiting the overall rate of carburization:

- lattice diffusion of reactant species through a dense, continuous, adherent, thickening carbide layer
- Grain boundary diffusion of reactant species through a carbide layer without grain growth

2.1.3 Cubic Rate Law

For some cases, grains of the carbide layer grow during carburization, and the diffusion of the reactant species through grain boundaries is the rate-limiting step. The parabolic rate law may no longer be valid in this case. A general form of the grain growth rate can be expressed as [31]

$$G^n - G_0^n = Kt \quad (\text{E3})$$

where G is the grain size, G_0 is the initial grain size, n is a power factor of grain growth, and K is the time-independent growth constant. If grains grow at cubic rates ($n = 3$), and grain boundary diffusion is much faster than lattice diffusion, the carburization rate can be expressed by the following equation:

$$\Delta x = \left(\frac{3k_{p,GB}}{K} \right)^{1/2} (kt + G_0^3)^{1/3} \quad (\text{E4})$$

where $k_{p,GB}$ is the rate constant associated with grain boundary diffusion. A cubic carburization law is obtained if grains grow at a cubic rate and grain boundary diffusion is the rate-limiting step.

2.1.4 Paralinear Rate Law

The paralinear carburization law can be expressed as [25].

$$\frac{d(\Delta x)}{dt} = \frac{k_p}{\Delta x} - k_l \quad \text{or} \quad t = \frac{k_p}{(k_l)^2} \left[-\frac{k_l}{k_p} \Delta x - \ln \left(1 - \frac{k_l}{k_p} \Delta x \right) \right] \quad (\text{E5})$$

where k_p and k_l are the parabolic rate constant and linear rate constant, respectively, Δx is the carbide film thickness, and t is the carburization time. The carburization follows initially a parabolic rate, when the carbide layer is relatively thin, and $\frac{k_p}{\Delta x}$ is much greater than k_l . Since Δx increases with time, $\frac{k_p}{\Delta x}$ decreases with time until $\frac{k_p}{\Delta x} = k_l$. The thickening rate becomes 0 at that time, and results in a constant carbide layer thickening and constant rate of weight loss. A paralinear rate law can occur due to the competition of two processes, such as

- Formation of a carbide layer by solid-state diffusion through the lattice at parabolic rate
- Destruction of the carbide layer at the gas/carbide interface by volatilization and migration of a gas species through a gas boundary layer of constant thickness

3. EXPERIMENTAL PROCEDURES

3.1 Reaction of W plates with pure CO gas

A pure tungsten sheet (99.95%, thickness of 1 mm) was obtained from a commercial source (Eagle Alloys, Talbott, TN, USA). The tungsten sheet was cut into 1.5 cm x 1.0 cm plates by using wire electrical discharge machining (Mitsubishi FX 20K wire EDM, Mitsubishi Electric Corporation, Tokyo, Japan). Both large area faces of the cut plates were first surface ground by a 600-grit grinding wheel and then polished to a surface finish of 1 μm by using a series of diamond pastes. The detailed polishing procedure is described in Table 1. The final thickness of the plates was 0.70 to 0.85 mm.

Table 1. Polishing procedure for pure tungsten plate samples.

Cloth	Abrasive	Lubricant	Time (min)
Grinding Wheel	600 – grit	Water	Until flat, about 5
PLAN-Cloth*	Diamond paste (9 μm)*	GreenLube*	10
PLAN-Cloth*	Diamond paste (3 μm)*	GreenLube*	10
DiaMat*	Diamond paste (1 μm)*	GreenLube*	5

*Allied High Tech Products, Inc., Rancho Dominguez, CA, USA

A research grade pure carbon monoxide gas was used as the carburizing gas (99.99% CO, Airgas, Kokomo, IN, USA). The plates were placed vertically on an alumina plate (McMaster-Carr, Princeton, Illinois, USA) by machining a 6.5 mm x 1.0 mm x 0.8 mm slot to allow for the fully exposure to the flowing CO gas during the reaction. The gap between the slot and the sample is in the range from 0.16 mm to 0.29 mm. The whole setup is shown in Figure 9.

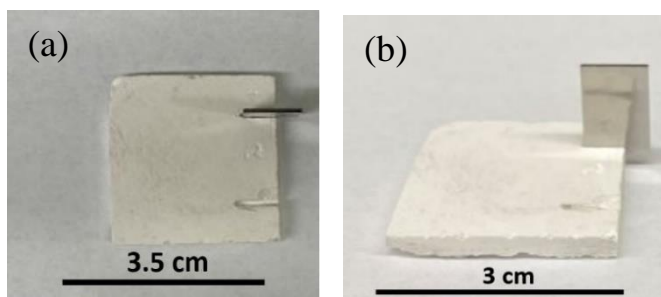


Figure 9. Photographs of the setup for W plate exposure to CO gas: (a) top view and (b) side view.

The plates were first heated in a horizontal tube furnace (Carbolite Gero, Newton, PA, USA) to 1000 °C under the 30 mL/min flow of ultra-high purity argon (99.999% Argon, Airgas, Kokomo, IN, USA) with a 6 °C/min heating rate. Once the furnace reached 1000 °C, the flowing gas was switched to pure CO gas, with a flow rate of 56.2 ml/min, for 12 h, 24 h, 36 h, 48 h, and 96 h. For each time, three samples were carburized. At last, the plates were cooled down in 30 mL/min flowing ultra-high purity argon (99.999%) with a 4 °C/min cooling rate.

3.2 Characterization of the carburized layer

Backscattered electron (BSE) images and energy dispersive X-ray (EDX) elemental maps of the two large area faces of the unreacted and reacted W plates were obtained using a scanning electron microscope (Phenom XL, Phenom-World BV, The Netherlands). To reveal the WC layer, the plates were across-sectioned using a focus ion beam (FIB) - equipped Quanta 3D FEG SEM (Thermo Fisher Scientific, Waltham, Massachusetts, USA). The average thickness of the WC layer, generated by the reaction of CO gas for a given time at 1000 °C, was determined from the FIB-cut cross-section at 15 different locations. TEM samples for tungsten plates carburized at 1000 °C for 12 h and 96 h were prepared by FIB and an Omniprobe 200 lift-out equipped (Oxford Instruments, Abingdon, UK) Quanta 3D FEG SEM. The FIB cut and TEM sample preparations were performed by Dr. Sunghwan Hwang. These samples were characterized using a Talos 200X TEM (Thermo Fisher Scientific, Waltham, Massachusetts, USA) operate at 200 kV (courtesy of Bo Yang).

X-ray diffraction (XRD) analyses were performed on all unreacted and reacted W plates using Cu K α radiation at 1.5406 Å over a 2 θ range from 20° to 90° with 0.02° step size and 0.2s step⁻¹ dwell time (Bruker D2 Phaser, Bruker AXS GmbH, Germany).

The surface roughness of the large face of the pure W plate and W plate carburized at 1000 °C for 12 h, 48 h, and 96 h were measured using an atomic force microscope (Digital Instruments, Santa Barbara, CA, USA) with a measuring range area of 25 μ m x 25 μ m.

The weight changes of the W plates due to the reaction with CO gas were measured by an electronic balance (ME36S, 0.001 mg resolution, Sartorius, Germany). The theoretical thickness of the reaction-formed WC films, calculated from the weight gain, was obtained using the following equation:

$$L = \frac{\frac{\Delta m}{m_C} \cdot m_{WC}}{\rho_{WC} \cdot A} \quad (E6)$$

where L is the average thickness of the layer, Δm is the weight gain, m_C is the atom mass of carbon, m_{WC} is the molecular weight of WC, ρ_{WC} is the density of WC (15.669 g/cm³) [32], and A is the total surface area exposed to the flowing gas.

3.3 Inert marker experiment

An inert marker experiment was conducted to determine the interface where the reaction occurred predominately. MgO particles (average size of 100 nm, 99% purity, Alfa Aesar, Haverhill, MA, USA) were selected as inert markers due to chemical compatibility with W, WC and CO (g). A mixture of 0.02 wt% MgO and hexane was sonicated to generate a suspension. Then the MgO particles were deposited onto the W plate surface by applying a drop of MgO/hexane suspension and allowing the hexane to evaporate. The deposited W plate was exposed to CO gas at 1000 °C for 96 h. The location of the MgO particles after the reaction was determined from BSE images and elemental maps of the surface and of a FIB-cut cross-section.

3.4 Preparation and Sintering of a Tungsten Wire Preform

Pure tungsten wire (99.95%, Midwest Tungsten Service, Willowbrook, IL, USA) with a diameter of 0.0005 in (0.0127 mm) was manually wound on a magnesia (MgO) plate. Figure 10 shows the setup for the wire winding and a photograph of the wound tungsten wire on the MgO plate. Two aluminum blocks were used as stands. A copper tube was placed through the center hole of the spool of the tungsten wire. The tube and spool were then placed on two aluminum blocks. Wires are wound on the MgO plate by rotating the plate. Once wound wires reach a certain thickness, the wound wires on the MgO plate were sintered in a graphite furnace (Oxy-Gon Industries, Inc., Epsom, NH, USA) under flowing Ultra-high purity argon (99.999%) to form rigid, bulk samples. The heating and cooling rates were both 15 °C/min, and samples were sintered at 1800 °C for 2 h. Sintered W wires samples were then removed from the MgO plates.

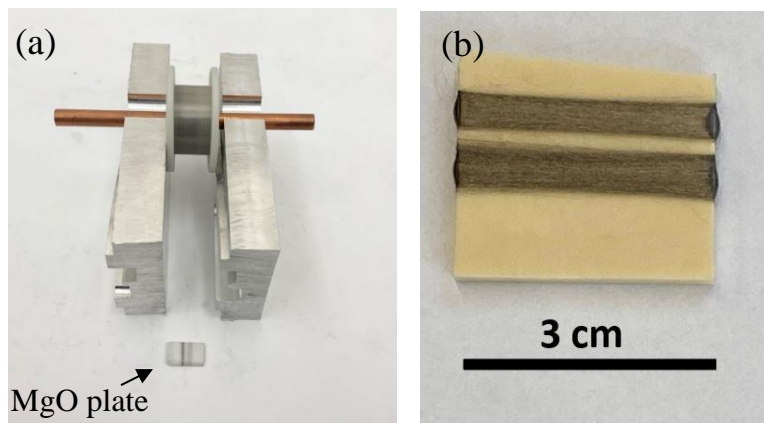


Figure 10. Photographs of (a) the assembly for winding the W wire on a MgO plate, and (b) the W wire wound on the MgO plate.

3.5 Carburization of Sintered Tungsten Wire

Sintered W wire samples were carburized using pure CO gas (99.99% CO, Airgas, Kokomo, IN, USA). Samples were heated in a horizontal tube furnace (Carbolite Gero, Newton, PA, USA) to 1000 °C with 30 ml/min flow of ultra-high purity argon (99.999%) at 6 °C/min heating rate. Then the flowing gas was switched to pure CO with a flow rate of 56.2 ml/min and the furnace temperature was fixed at 1000 °C for 96 h. Samples were cooled down to room temperature in the 30 ml/min flowing ultra-high purity argon (99.999%) at a 4 °C/min cooling rate.

3.6 Preparation of the Zr₂Cu alloy

Zr₂Cu alloy was prepared in a water-cooled graphite furnace (Oxy-Gon Industries, Inc., Epsom, NH, USA). A 1.0 mm x 6.1 mm Zr piece was cut from a Zr sheet with 0.635 mm thickness (0.024933g, 99.2%, Eagle Alloys, Talbott, TN, USA) and a 1.0 mm x 1.5 mm Cu piece was cut from a Cu sheet with 0.635 mm thickness (0.0085g, 99.9% purity, McMaster-Carr, Atlanta, GA). Both cut Cu and Zr pieces were placed in a 0.5 in x 1.0 in magnesia (MgO) crucible (Tateho Ozark Ceramics, Inc., MO, USA). Cu was placed on top of the Zr due to its higher density and lower melting point, which helped the alloying. Prior to melting, the chamber of the graphite furnace was evacuated and backfilled with ultra-high purity (99.999%) argon three times to remove the residual oxygen. The furnace was then heated to 1150 °C and held for 10 min for alloying of zirconium and copper. At last, the furnace was cooled down to room temperature. The heating and cooling

rates were both 15 °C/min. The whole process was conducted under the 1L/min flow of ultra-high purity argon (99.999%).

3.7 Infiltration of Tungsten Wire Sample

The prepared Zr_2Cu alloy was placed at the bottom of the MgO crucible. The tungsten wire preform was placed in the MgO crucible in contact with the solid Zr_2Cu alloy. A schematic illustration of the assembly is shown in Figure 11. The sample was then heated in a water-cooled graphite furnace (Oxy-Gon Industries, Inc., Epsom, NH, USA). Similar to the Zr_2Cu preparation, evacuation and Ar backfilling were conducted three times to remove the residual oxygen. The sample was heated to 1350 °C and held for 10 min to allow for the reaction between WC (s) and Zr_2Cu (l). The assembly was then cooled to room temperature. The whole process was conducted under the flow of ultra-high purity argon (99.999%). The heating and cooling rates were both 15 °C/min.

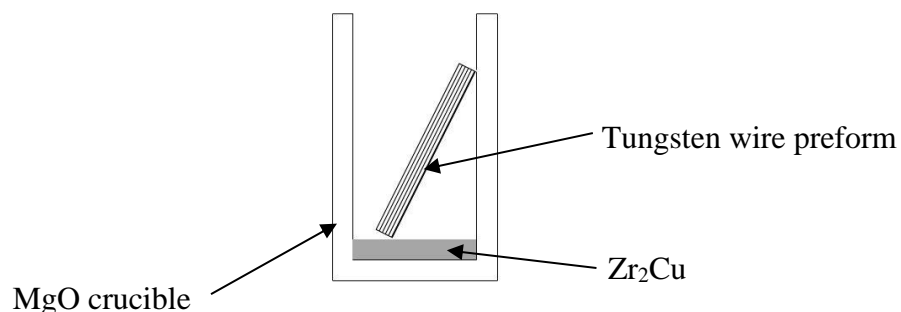


Figure 11. Schematic illustration of the setup for tungsten wire preform infiltration.

3.8 Characterization of Tungsten Wire Sample

Backscattered electron (BSE) images of the W wire sample after sintering were obtained with a scanning electron microscope (Phenom XL, Phenom-World BV, The Netherlands). Backscattered electron (BSE) images and energy dispersive X-ray (EDX) elemental maps of W wire samples after reactive Zr_2Cu infiltration were obtained using a Quanta 3D FEG SEM (Thermo Fisher Scientific, Waltham, Massachusetts, USA). X-ray diffraction (XRD) analyses were performed on the W wire sample after sintering and infiltration using Cu $K\alpha$ radiation at 1.5406 Å over a 2θ range from 20° to 90° with 0.02° step size and 0.2s step^{-1} dwell time (Bruker D2 Phaser, Bruker AXS GmbH, Germany).

4. RESULTS AND DISCUSSION

4.1 Kinetic Mechanism of Tungsten Carburization with CO Gas

A SE image of the unreacted W plate and its associated elemental map from the surface are shown in Figure 12. Only W was detected on the surface of the sample by EDX analysis. Figure 13 shows the XRD pattern of the same unreacted specimen. Only peaks associated with tungsten were detected, which was consistent with the EDX analysis. The average surface roughness was measured as 7.3 ± 0.8 nm by an atomic force microscope (AFM). The AFM image of the surface is shown in Figure 14. The bulk density of the sample was measured to be 18.51 ± 0.36 g/cm³, which corresponded to 96.1% of the theoretical density for tungsten (19.26 g/cm³) [33]. No visible cracks were observed on the W plate sample surfaces. Hence, samples used for the carburization kinetic study were dense with smooth polished surfaces.

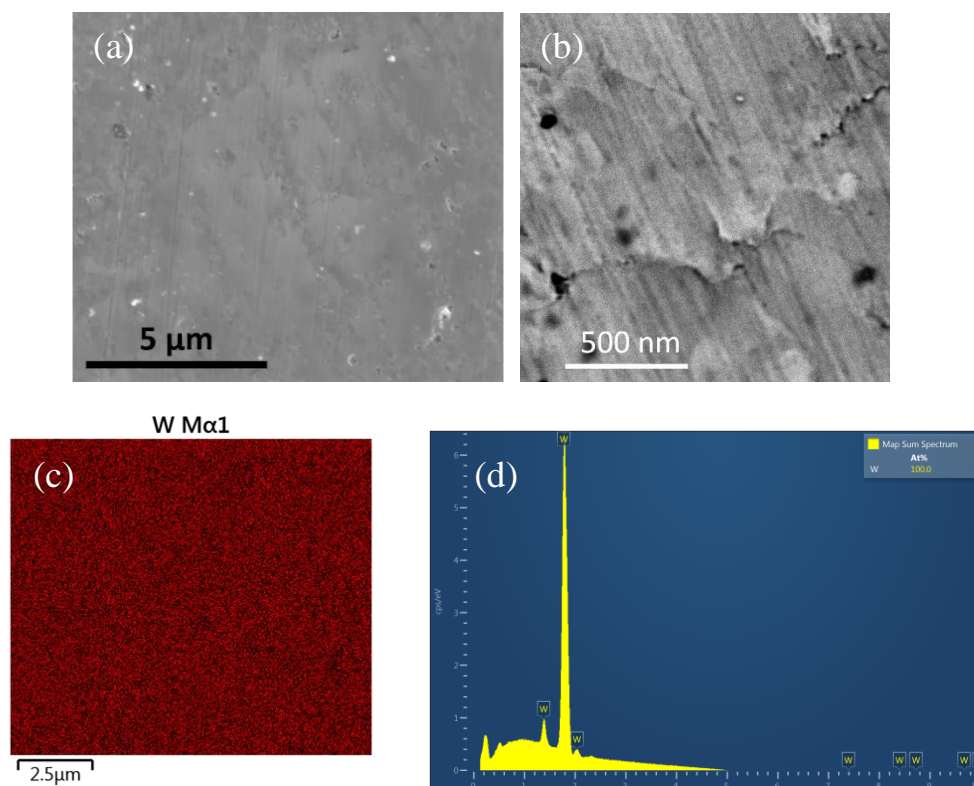


Figure 12. SE images of the polished surface of the pure tungsten plate at (a) a lower magnification and (b) a higher magnification and associated elemental map of (c) tungsten, and (d) the EDX spectrum.

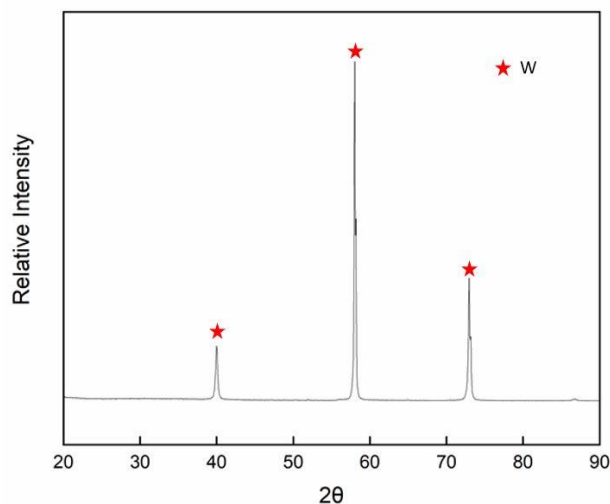


Figure 13. XRD pattern obtained from the polished surface of the unreacted tungsten plate

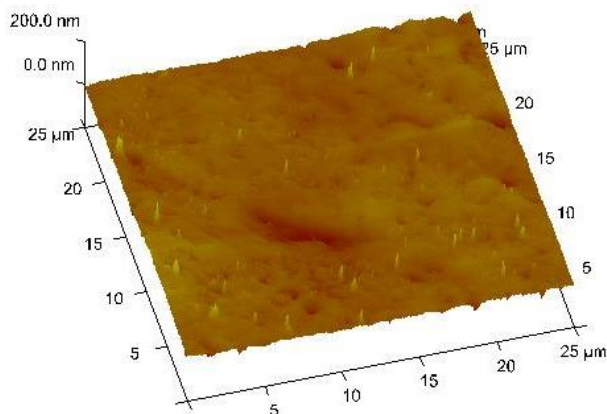


Figure 14. AFM image (25 μm x 25 μm) of the surface roughness of the pure W plate.

SE images of surfaces of W plates and their associated elemental maps after reaction with pure CO gas at 1000 °C for 12 h, 24 h, 36h, 48 h, and 96 h are shown in Figure 15 to Figure 19. All of these specimen surfaces show polycrystalline surfaces without apparent macrocracks. The EDX analyses indicated only tungsten and carbon on specimen surfaces. XRD patterns from surfaces were obtained for W plates after exposure to CO gas from 12 h to 96 h at 1000 °C, as shown in Figure 20. For all reaction times, only WC peaks and W peaks were detected.

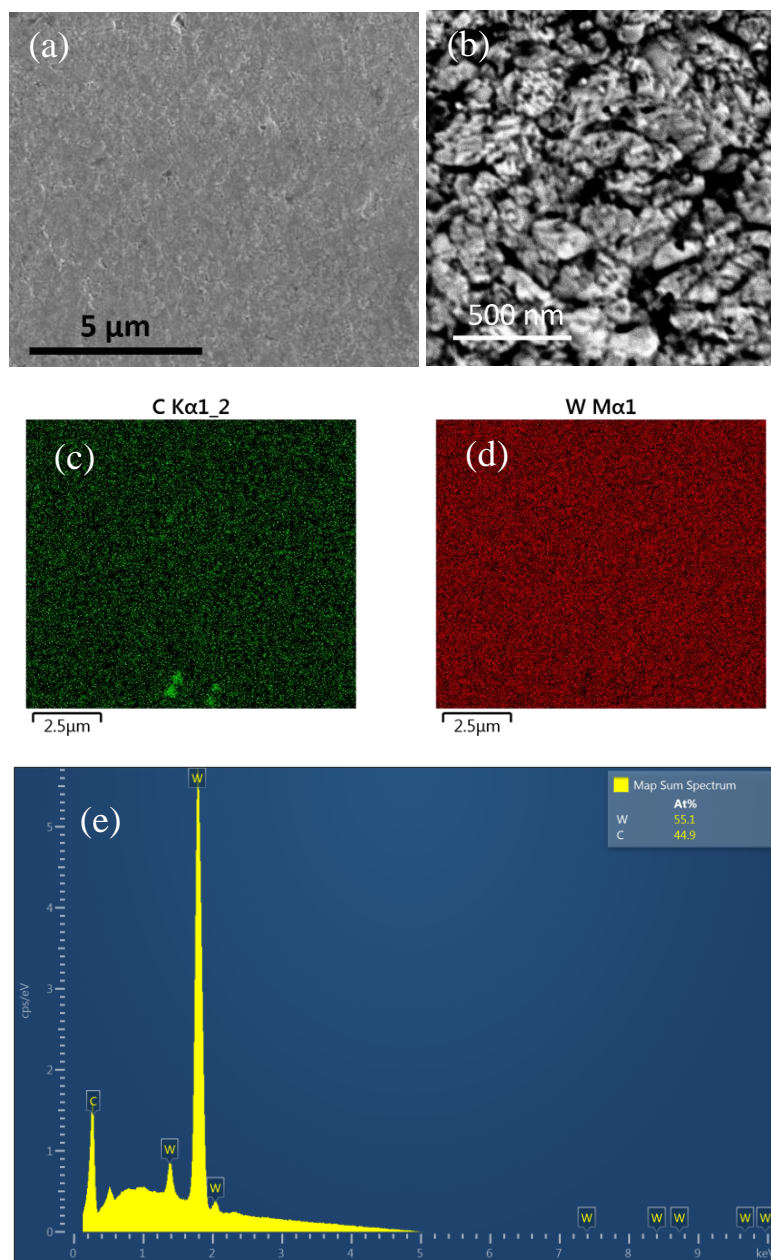


Figure 15. SE images of the polished surface of the pure tungsten plate at (a) a lower magnification and (b) a higher magnification and associated elemental maps of (c) carbon and (d) tungsten after reaction with pure CO gas at 1000 $^{\circ}\text{C}$ for 12 h, and (e) the EDX spectrum.

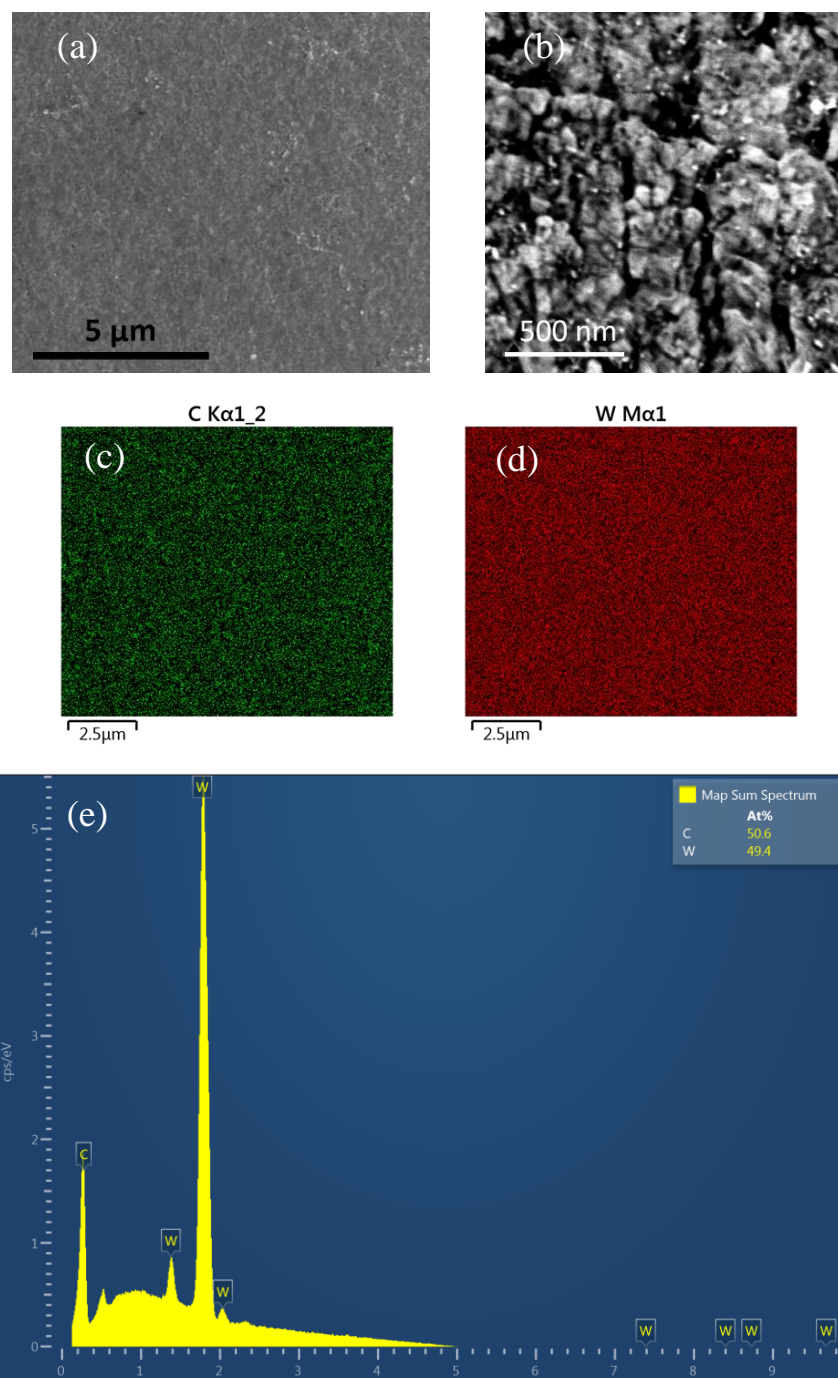


Figure 16. SE images of the polished surface of the pure tungsten plate at (a) a lower magnification and (b) a higher magnification and associated elemental maps for (c) carbon and (d) tungsten after reaction with pure CO gas at 1000 $^{\circ}\text{C}$ for 24 h, and (e) the EDX spectrum.

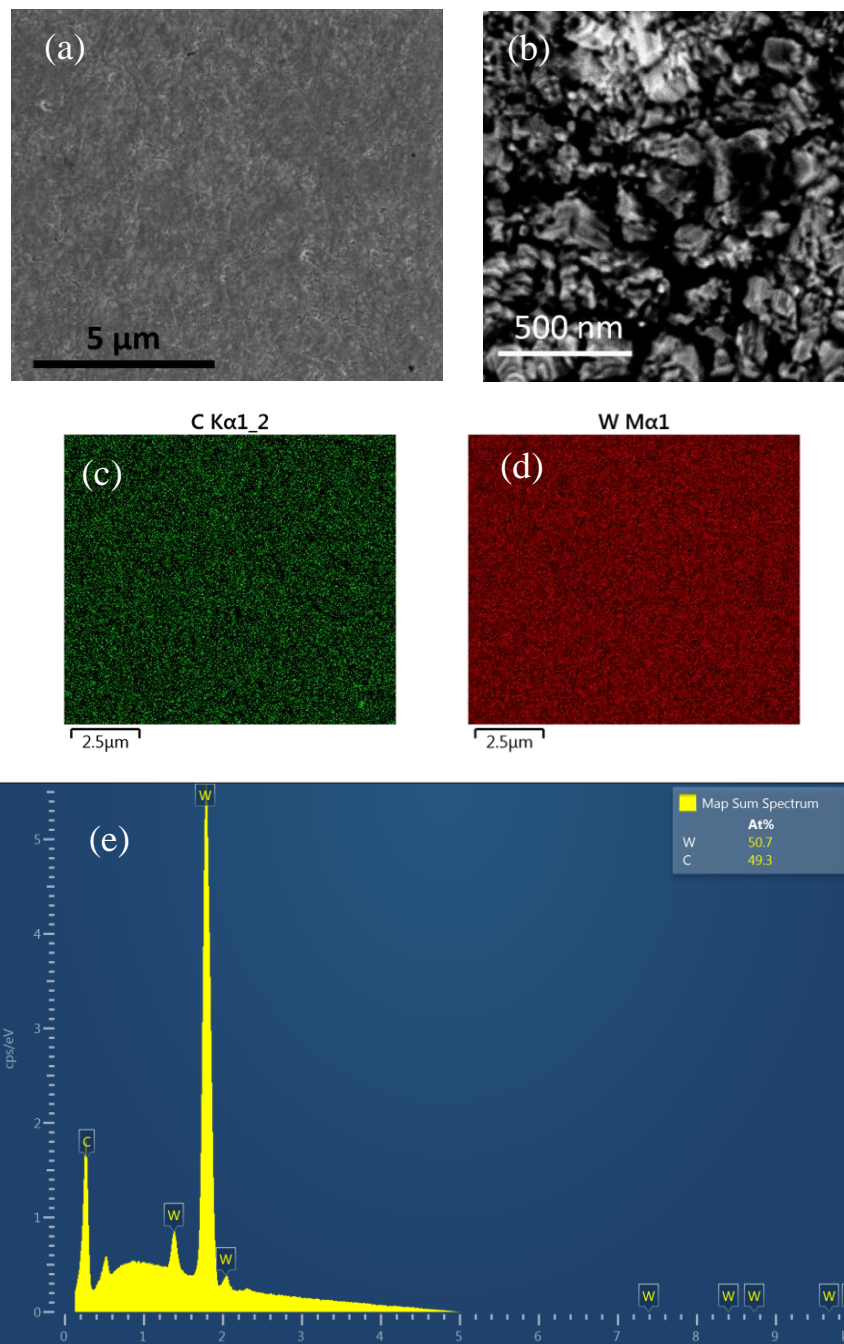


Figure 17. SE images of the polished surface of the pure tungsten plate at (a) a lower magnification and (b) a higher magnification and associated elemental maps for (c) carbon and (d) tungsten after reaction with pure CO gas at 1000 °C for 36 h, and (e) the EDX spectrum.

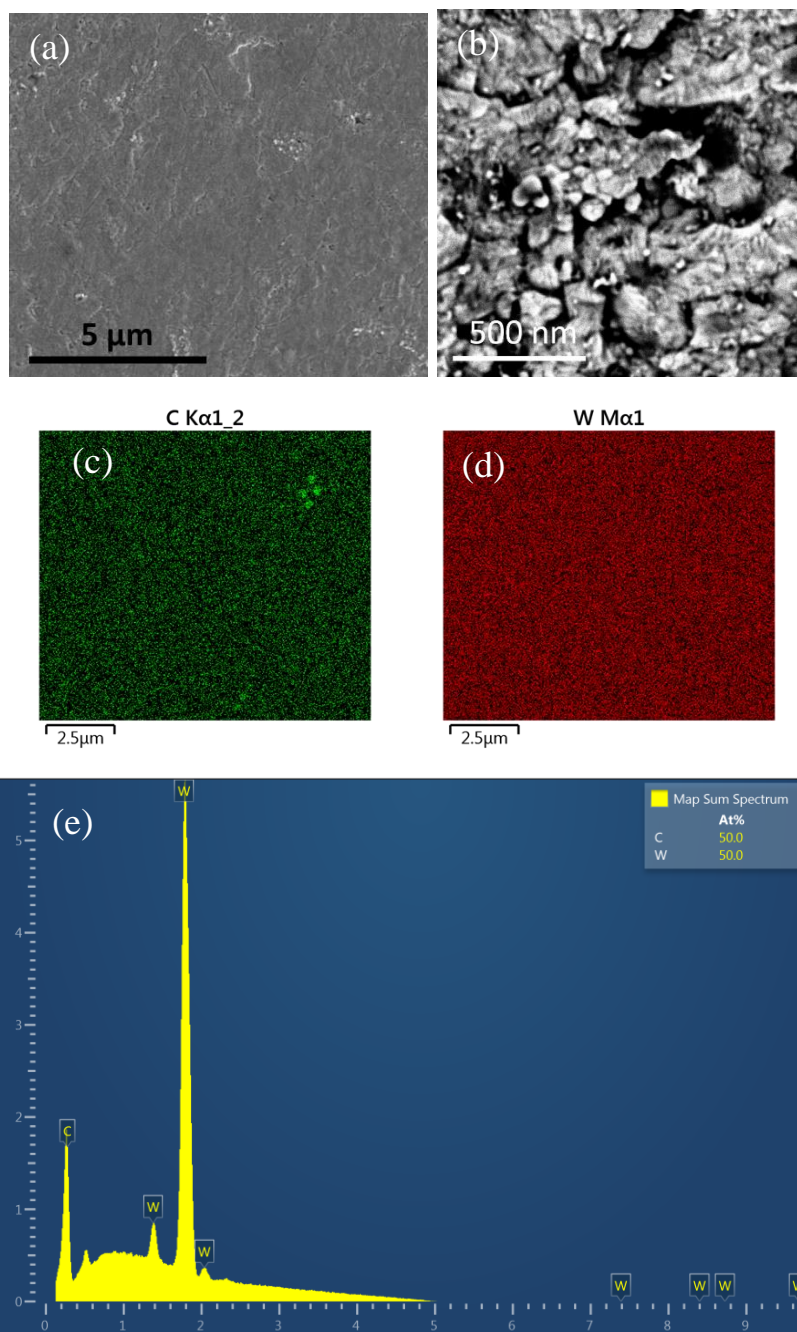


Figure 18. SE images of the polished surface of the pure tungsten plate at (a) a lower magnification and (b) a higher magnification and associated elemental maps for (c) carbon and (d) tungsten after reaction with pure CO gas at 1000 $^{\circ}\text{C}$ for 48 h, and (e) the EDX spectrum.

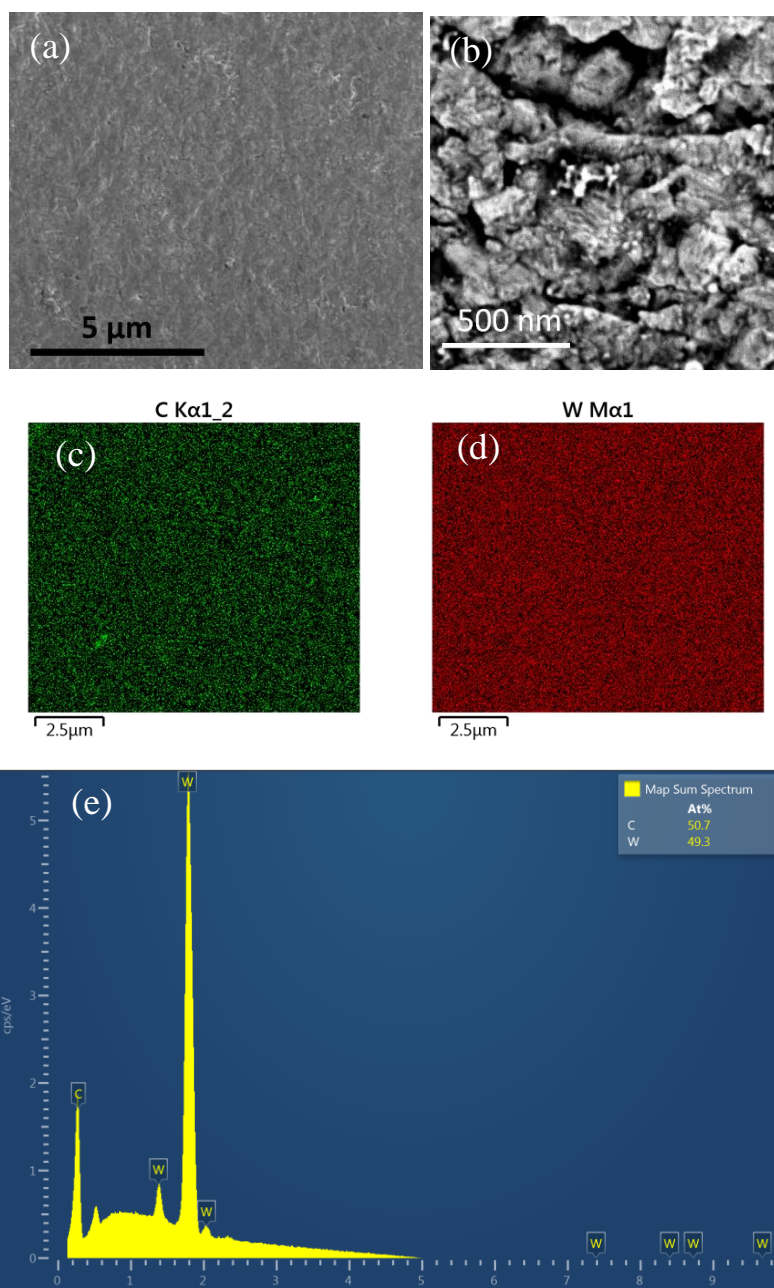


Figure 19. SE images of the polished surface of the pure tungsten plate at (a) a lower magnification and (b) a higher magnification and associated elemental maps for (c) carbon and (d) tungsten after reaction with pure CO gas at 1000 $^{\circ}\text{C}$ for 96 h, and (e) the EDX spectrum.

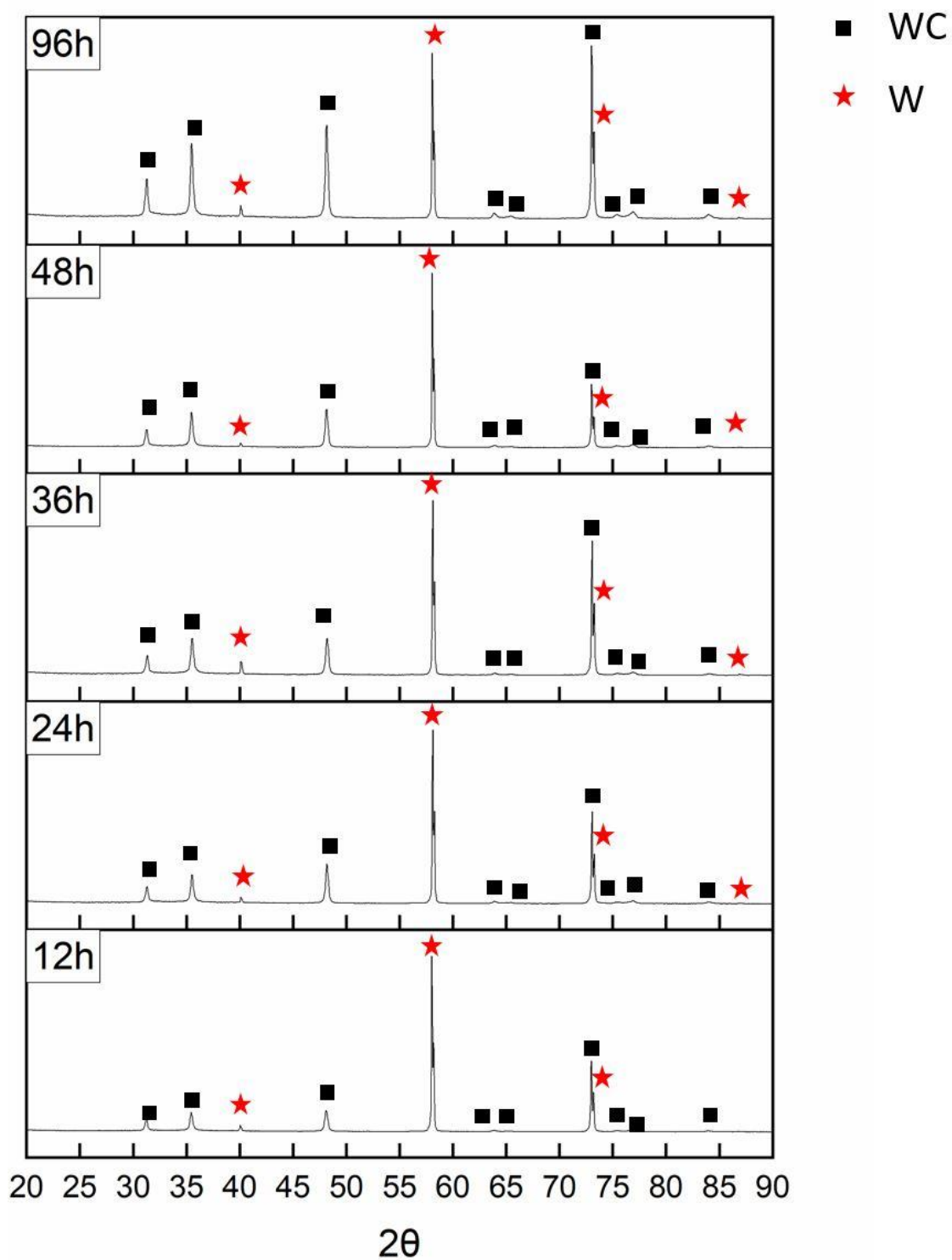


Figure 20. XRD patterns obtained from surfaces of W plates after reaction with pure CO gas at 1000 °C for 12 to 96 h.

The average surface roughness values of the large faces of the W plates before and after reaction with CO gas at 1000 °C for 12 h, 48 h, and 96 h were measured by AFM. AFM images are shown in Figure 21 and surface roughness values are listed in Table 2. The surface roughness of the W plate exhibited a positive correlation with reaction times. The formation of the WC film roughened the surface of the W plate, and the surface roughness increases with the increase of the reaction time.

Table 2. Surface roughness of the large face of the unreacted W plates and reacted with CO gas at 1000 °C for 12 h, 48 h, and 96 h.

Reaction Time (h)	Surface Roughness (nm)
0	7.3 ± 0.8
12	15.3 ± 0.8
48	16.2 ± 0.4
96	17.8 ± 0.8

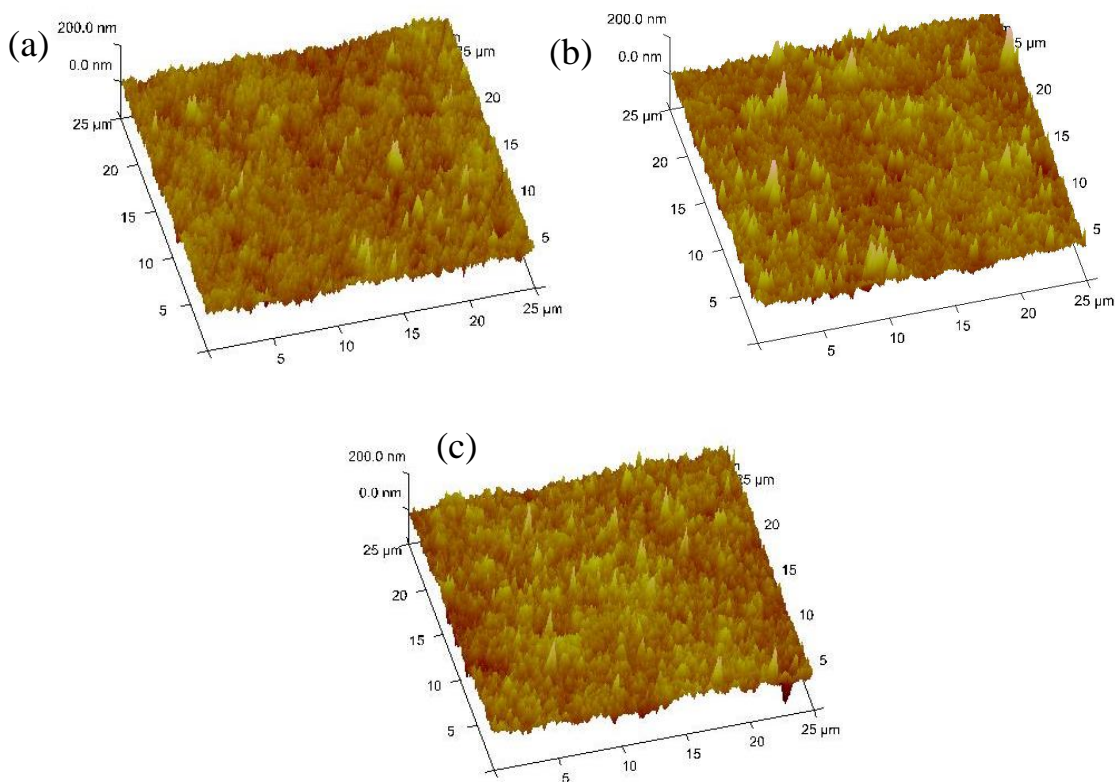


Figure 21. AFM images (25 μm x 25 μm) of the surface roughness of W plates after reaction with pure CO gas at 1000 °C for (a) 12 h, (b) 48 h, and (c) 96 h.

To further characterize the WC film formed on the W plate after exposure to pure CO gas at 1000 °C, TEM analyses were conducted on a sample after 12 h of carburization. Figure 22 shows the STEM image including the layer and the substrate, and SAED patterns from the layer and substrate areas. The SAED pattern from the layer area matched with the hexagonal structure of WC [32], and the SAED pattern from the matrix area matched with the cubic structure of W [33]. W_2C , another stable carbide with W, was not detected between the WC/W interface. EDX, XRD and TEM analyses of the carburized W plate confirmed pure tungsten could be converted into WC by reaction with pure CO gas at 1000 °C.

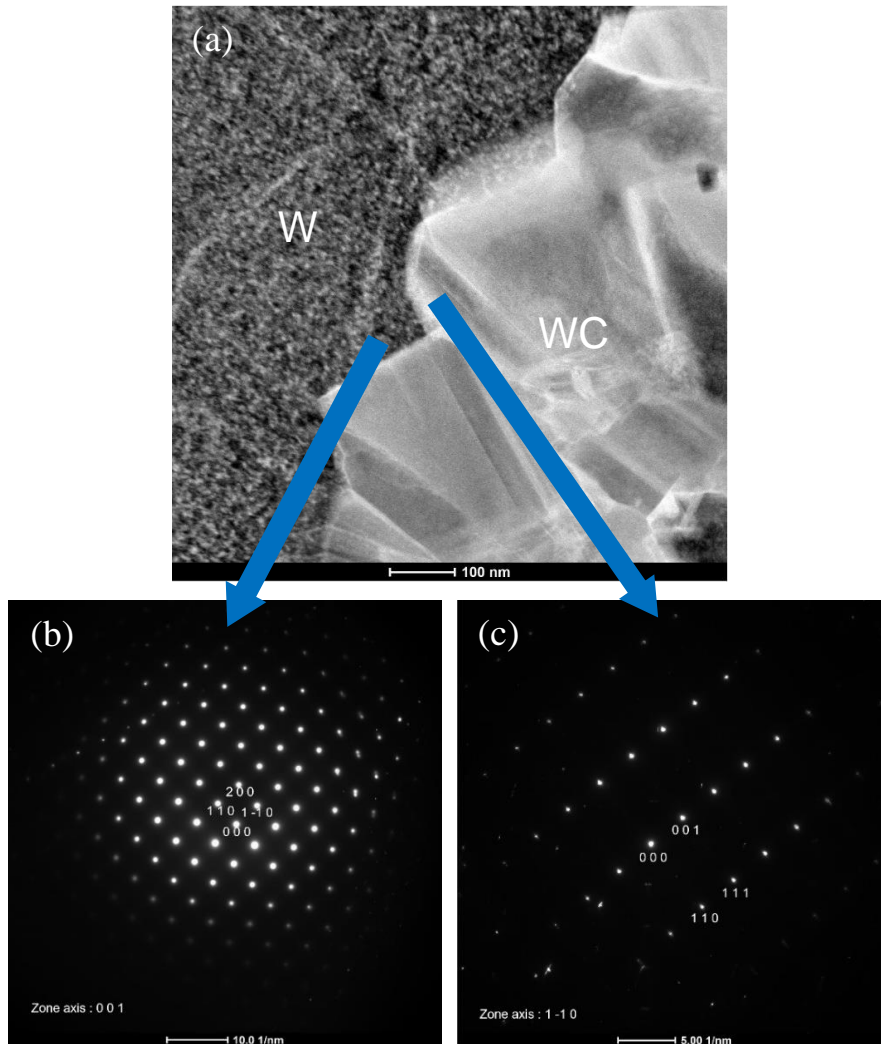
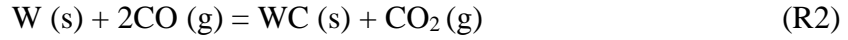


Figure 22. (a) STEM image of the ion-milled cross-section of the tungsten plate after reaction with pure CO gas at 1000 °C for 12 h showing a WC layer and W substrate, and the SAED pattern from (b) the tungsten substrate with a zone axis of [001] and from (c) the WC layer with a zone axis of [110] (Courtesy of Bo Yang)

The following reaction can be considered as the overall net reaction during the carburization of W to form WC films:



Another possible reaction is the formation of a W₂C film instead of WC. This reaction is shown below:



Understanding the equilibrium partial pressure $P_{\text{CO}_2}/P_{\text{CO}}$ ratio is important to determine which reaction may happen at a certain temperature. The equilibrium $P_{\text{CO}_2}/P_{\text{CO}}$ ratio can be calculated using the following equation:

$$\Delta G^\circ = -RT \ln K \quad (\text{E7})$$

where ΔG° is the standard Gibbs free energy change of a reaction, R is the ideal gas constant (8.3145 J/mol⁻¹K⁻¹) and K is the equilibrium reaction quotient. All solid species in these reactions are assumed to be pure and WC is assumed to be stoichiometric carbide. If ideal gas species at 1 atm pressure are assumed along with pure solid reference states, K can be represented by the partial pressure ratio of CO and CO₂, $\frac{P_{\text{CO}_2}}{(P_{\text{CO}})^2}$, for both reactions. ΔG° for all three reactions at 1200 K and 1300 K were calculated according to thermodynamic data from the literature [34] as shown in Table 3. Since data for the actual experimental temperature 1273 K (1000 °C) are not available, a linear relationship with temperature was assumed to estimate ΔG° at 1273 K.

Table 3. Calculated ΔG° values for Rxn. (R2) and (R3) at 1200 K, 1273 K, and 1300 K.

Temperature (K)	$\Delta G^\circ_{\text{rxn 2}}$ (kJ/mol)	$\Delta G^\circ_{\text{rxn 3}}$ (kJ/mol)
1200	4.281	13.623
1300	21.825	29.145
1273	17.088	24.954

If the sum of P_{CO_2} and P_{CO} is assumed to equal 1 atm, then the equilibrium partial pressure $P_{\text{CO}_2}/P_{\text{CO}}$ for each reaction can be calculated, and these values are shown in Table 4. ΔG needs to be negative for these reactions to proceed spontaneously to the right, which means a lower partial pressure $P_{\text{CO}_2}/P_{\text{CO}}$ than the equilibrium ratio is needed. The source gas used in the experiment was 99.99% CO with 5 ppm oxygen and 40 ppm nitrogen. CO₂ was introduced to the gas via the following reaction:



Assuming P_{co} equals 0.9999 atm and P_{O_2} equals 5×10^{-6} atm, and O_2 is completely reacted with CO, the content of produced CO_2 from reaction 4 equals 10 ppm. Partial pressure ratio $P_{\text{CO}_2}/P_{\text{co}}$ was then determined as 1×10^{-5} for the supply gas in the tube furnace during the carburization. The value was lower than for both Rxn. (R2) and (R3). ΔG values for both reactions were then calculated using Eq. (E8) as listed in Table 5, where Q is the reaction quotient. Negative values of ΔG for Rxn. (R2) and (R3) indicate that both reactions are favorable to proceed to the right at 1000 °C for the CO gas used in this experiment. Moreover, Rxn. (R2) is slightly more favored compared to Rxn. (R3) at 1000 °C due to a more negative ΔG value.

$$\Delta G = \Delta G^0 + RT \ln Q \quad (\text{E8})$$

Table 4. The equilibrium partial pressure $P_{\text{CO}_2}/P_{\text{co}}$ for Rxn. (R2) and (R3) at 1273 K.

Temperature (K)	$P_{\text{CO}_2}/P_{\text{co}}_{\text{rxn2}}$	$P_{\text{CO}_2}/P_{\text{co}}_{\text{rxn3}}$
1273	0.170	0.087

Table 5. ΔG values for Rxn. (R2) and (R3) at 1273 K

Temperature (K)	ΔG_{rxn2} (kJ/mol)	ΔG_{rxn3} (kJ/mol)
1273	-104.761	-96.895

Average values of the mass change per area ($\Delta m/A$) for W plates carburized using CO gas at 1000 °C for 12 to 96 h are provided in Table 6. The average values were obtained from three repetitive experiments at each time. Figure 23 shows the plot of the mass change per area ($\Delta m/A$) versus time. A non-linear power law relation between two variables was found. Chemical reaction control and gas phase diffusion control are excluded from the possible rate-limiting steps since both of these rate-limiting steps should yield a linear rate law between the mass change per unit area and time for the carburized W plates. A plot of the logarithm of the mass change per unit area ($\Delta m/A$) versus the logarithm of the reaction time is shown in Figure 24. The best linear fit line gives a slope of 0.344 ± 0.0467 with a R^2 value of 0.982. The slope of this plot falls between slopes representing the parabolic rate law and cubic rate law, which are 1/2 and 1/3 for their logarithm plots, respectively. Figure 25 and Figure 26 show plots of mass change per unit area versus time to the power of 1/2 and the time to the power of 1/3, respectively. The values of R^2 of the best

linear fit lines are 0.930 and 0.955 for the plot with time to the power of 1/2 and with time to the power of 1/3, respectively. The mass change data fits slightly better to the cubic rate law.

Table 6. Mass change per area versus reaction time data for W plates reacted with pure CO gas at 1000 °C for 12 to 96 h.

No.	Time (h)	Length (cm)	Width (cm)	Thickness (mm)	Total surface area (cm ²)	Total exposed surface area, A (cm ²) ^a	Δm (mg)	Δm/A (mg/cm ²)
1	12	1.50	1.00	0.78	3.39	3.21	0.153	0.048
2	12	1.50	1.00	0.76	3.38	3.20	0.164	0.051
3	12	1.50	1.00	0.75	3.37	3.19	0.149	0.047
Average Δm/A with 95% confidence range								0.049 ± 0.003
4	24	1.50	1.00	0.83	3.42	3.23	0.233	0.072
5	24	1.50	1.00	0.80	3.40	3.22	0.228	0.071
6	24	1.50	1.00	0.84	3.42	3.24	0.207	0.064
Average Δm/A with 95% confidence range								0.069 ± 0.006
7	36	1.50	1.00	0.82	3.41	3.23	0.271	0.084
8	36	1.50	1.00	0.71	3.36	3.17	0.25	0.079
9	36	1.50	1.00	0.84	3.42	3.24	0.239	0.074
Average Δm/A with 95% confidence range								0.079 ± 0.007
10	48	1.50	1.00	0.83	3.41	3.23	0.268	0.083
11	48	1.50	1.00	0.82	3.41	3.23	0.277	0.086
12	48	1.50	1.00	0.81	3.41	3.22	0.287	0.089
Average Δm/A with 95% confidence range								0.086 ± 0.004
13	96	1.50	1.00	0.80	3.40	3.22	0.3	0.093
14	96	1.50	1.00	0.73	3.36	3.18	0.3	0.094
15	96	1.50	1.00	0.79	3.39	3.21	0.33	0.103
Average Δm/A with 95% confidence range								0.097 ± 0.007

± refers to the 95% confidence limit range of thickness Δm/A values

^a Total surface area of samples excluded the area of the 6.5 mm x 1.0 mm x 0.8 mm slot

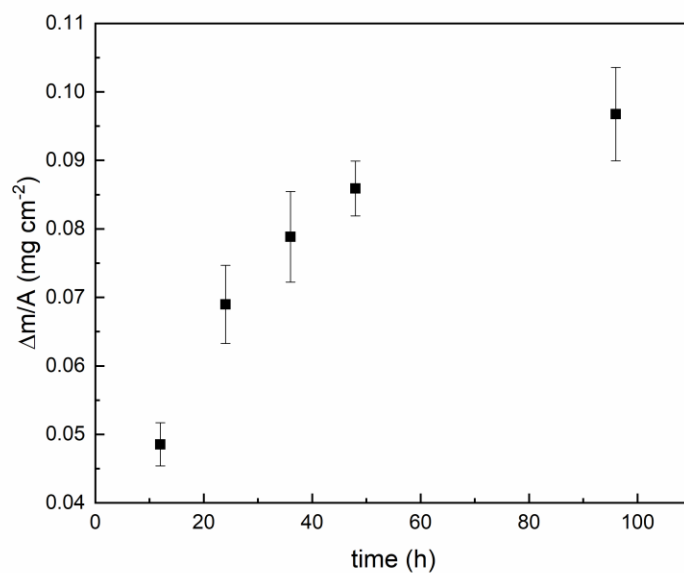


Figure 23. Plot of the mass change per area versus reaction time for W plates after reaction with pure CO gas at 1000 °C for 12 to 96 h.

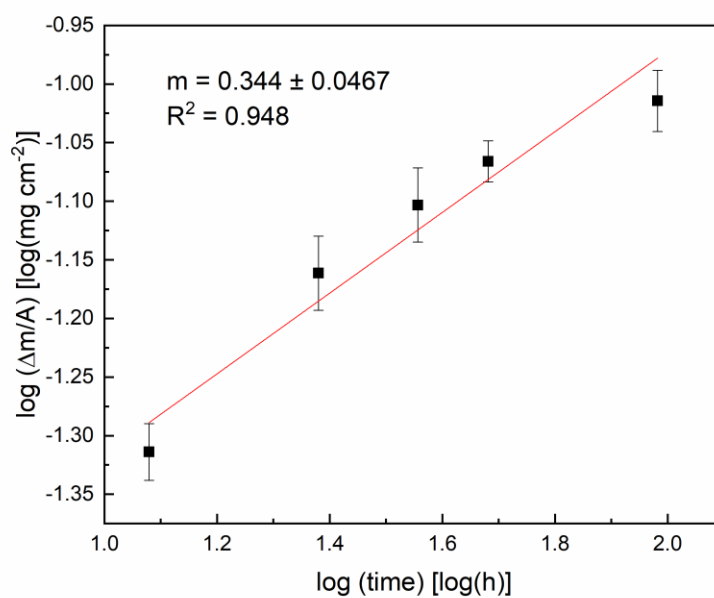


Figure 24. Plot of the log (mass change per area) versus log (reaction time) for W plates after reaction with pure CO gas at 1000 °C for 12 to 96 h.

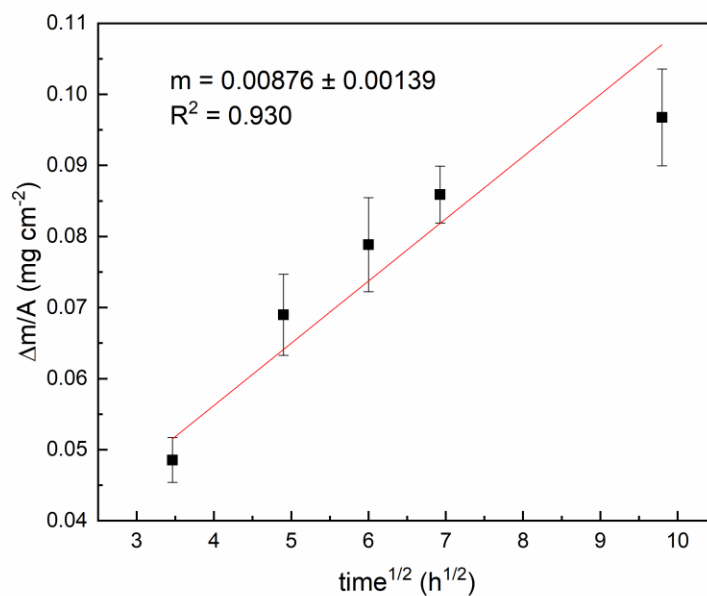


Figure 25. Plot of the mass change per area versus time^{1/2} for W plates after reaction with pure CO gas at 1000 °C for 12 to 96 h.

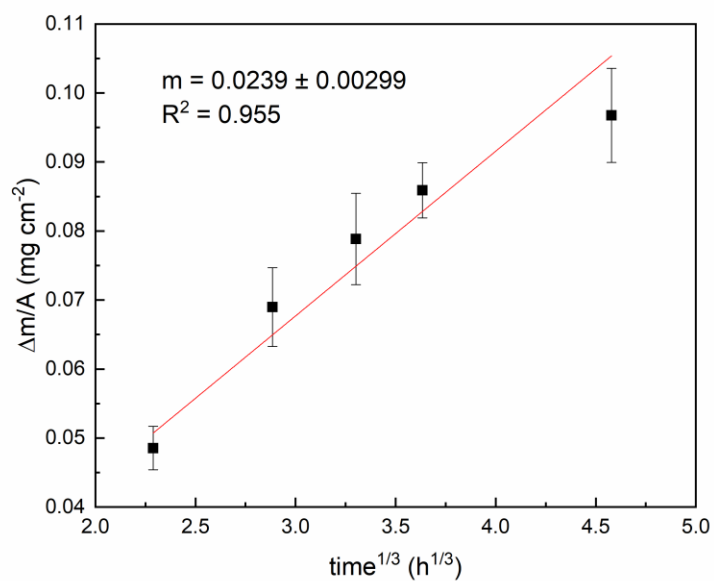


Figure 26. Plot of the mass change per area versus time^{1/3} for W plates after reaction with pure CO gas at 1000 °C for 12 to 96 h.

The average thicknesses of WC films were measured from BSE images of the FIB-cut cross-sections at 15 different locations for each reaction time. For example, Figure 27 shows two FIB-cut cross-sections for the W plate after exposure to CO gas at 1000 °C for 24 h. The thickness of the film was measured from 15 different locations as labeled in Figure 27. An average of $792 \text{ nm} \pm 50 \text{ nm}$ of the film thickness was obtained. Measured thicknesses of WC films and theoretical thickness calculated using Eq. (E6) for W plates carburized with CO gas at 1000 °C for 12 to 96 h are collected in Table 7. Calculated values of the film thickness and direct measurements show a good agreement.

Table 7. Thickness of the WC film versus reaction time data for W plates reacted with pure CO gas at 1000 °C for 12 to 96 h.

Time (h)	Measure thickness (nm)	Theoretical thickness (nm)
12	524 ± 15	539
24	792 ± 66	773
36	900 ± 48	880
48	1019 ± 101	927
96	1258 ± 73	1108

\pm refers to the 95% confidence limit range of thickness values

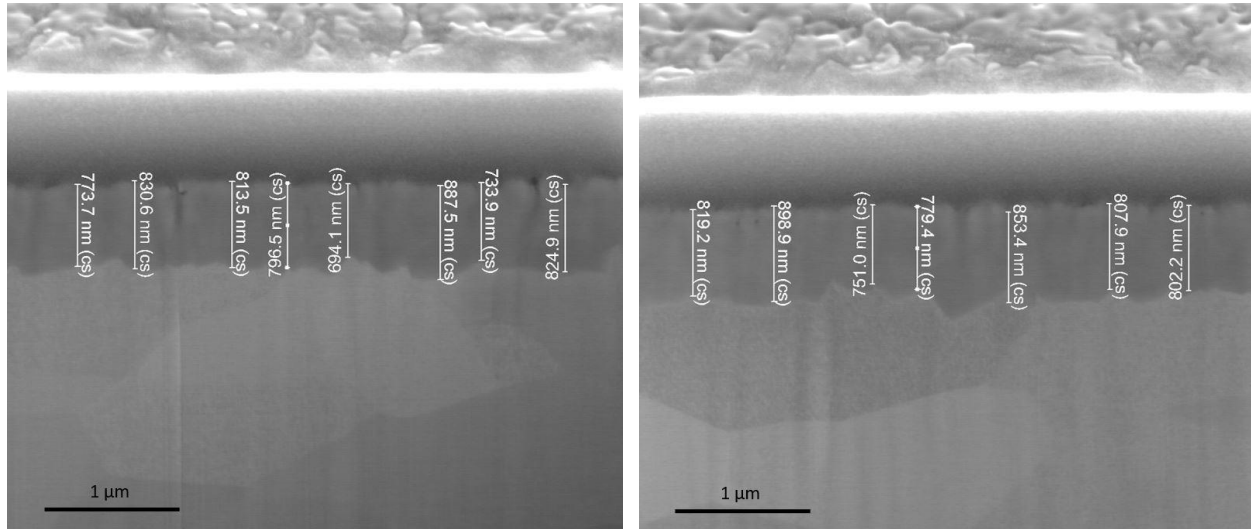


Figure 27. SEM image of the FIB-cut cross-section of the W plate after reaction with pure CO gas at 1000 °C for 24 h. The thickness of the film was determined by measuring at 15 different locations as labeled in the image above. (FIB cut was operated by Dr. Sunghwan Hwang)

High resolution BSE images of FIB-cut cross-sections and of surfaces for W plates after exposure to CO gas at 1000 °C for 12 to 96 h are shown from Figure 28 to Figure 32. The reacted WC films were dense and continuous. The platinum layers shown in all images were deposited to protect the WC during the FIB-cutting.

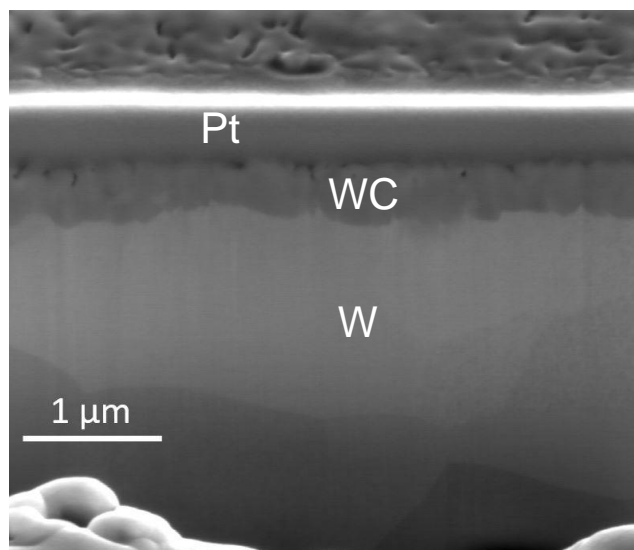


Figure 28. High resolution SE images of the FIB-cut cross-section of the W plate reacted with pure CO gas at 1000 °C for 12 h. (FIB cut was operated by Dr. Sunghwan Hwang)

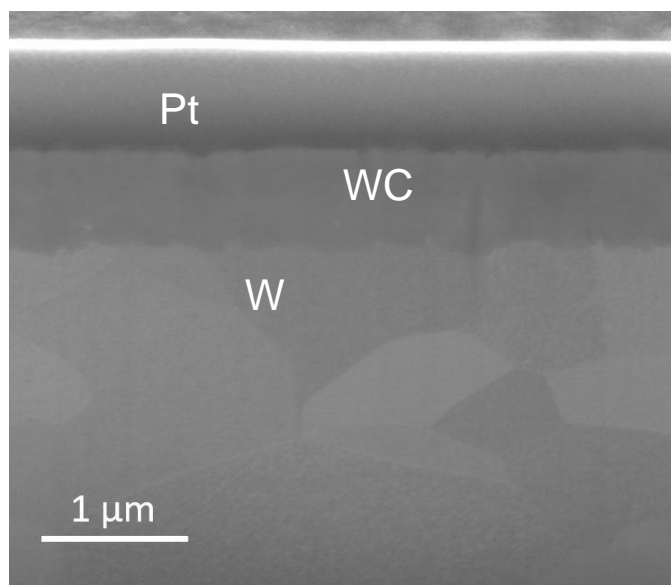


Figure 29. High resolution SE images of the FIB-cut cross-section of the W plate reacted with pure CO gas at 1000 °C for 24 h. (FIB cut was operated by Dr. Sunghwan Hwang)

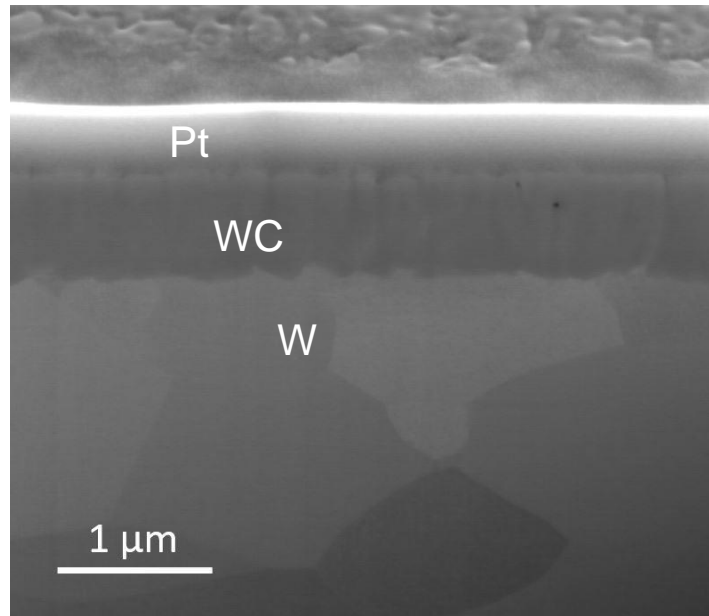


Figure 30. High resolution SE images of the FIB-cut cross-section of the W plate reacted with pure CO gas at 1000 °C for 36 h. (FIB cut was operated by Dr. Sunghwan Hwang)

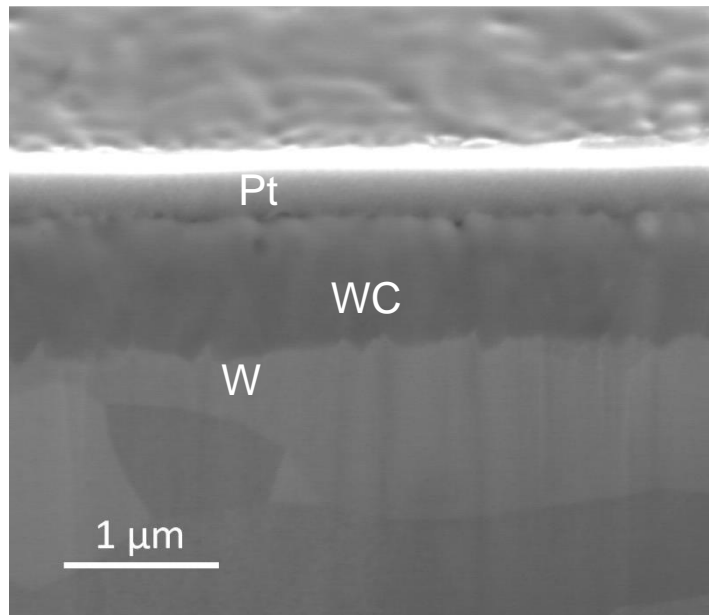


Figure 31. High resolution SE images of the FIB-cut cross-section of the W plate reacted with pure CO gas at 1000 °C for 48 h. (FIB cut was operated by Dr. Sunghwan Hwang)

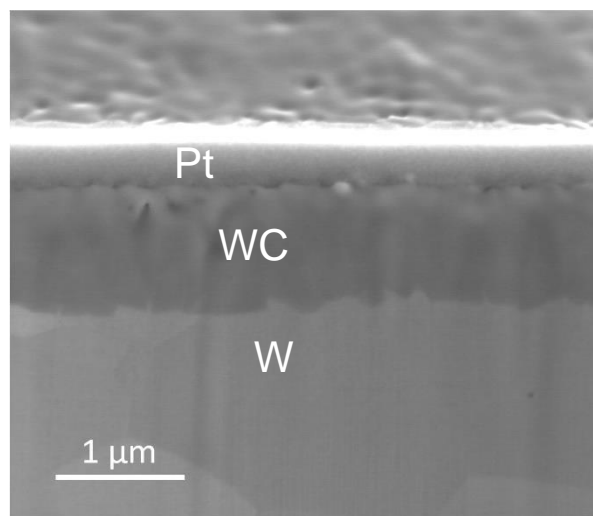


Figure 32. High resolution SE images of the FIB-cut cross-section the W plate reacted with pure CO gas at 1000 °C for 96 h. (FIB cut was operated by Sunghwan Hwang)

A plot of average WC film thickness versus reaction time is shown in Figure 33 for W plates reacted with CO gas at 1000 °C for 12 to 96 h. Similar to the plot for the mass change per unit area versus reaction times in Figure 23, a non-linear power law relation was found between the WC film thickness and reaction time. A logarithm plot of WC film thickness versus reaction time is shown in Figure 34, where the best linear fit line gives a slope of 0.439 ± 0.029 with a R^2 value of 0.987. The slope, similar to the value found from the mass change data, also indicates that the thickening rate of the WC film formation via the reaction between W and CO gas falls between the parabolic rate law and cubic rate law. Figure 35 and Figure 36 show plots of WC film thickness versus $\text{time}^{1/2}$ and $\text{time}^{1/3}$, respectively. The values of R^2 of the best lines are 0.977 and 0.989 for the plot with time to the power of $1/2$ and with time to the power of $1/3$, respectively. Thickness data have a better linear fit with time to the power of $1/3$, which were consistent with weight change data. In addition, formed WC films were dense and continuous as observed from SE images shown in Figure 28 to Figure 32, which met all assumptions for both parabolic rate law and cubic rate law. Three assumptions for the kinetic mechanism of W carburization with CO gas can be made here. First, the W carburization with CO gas at 1000 °C is controlled by lattice diffusion of reactant species through the WC film. Second, the W carburization with CO gas is controlled by grain boundary diffusion of reactant species through the WC film and slightly grain growth of the WC film. Third, the W carburization with CO gas is controlled by the combination of lattice diffusion and grain boundary diffusion of reactant species through the WC film and slightly grain

growth of the WC film. The last two assumptions are valid if a significant grain growth with reaction time for the WC film could be observed. Second, the W carburization with CO gas is controlled by the combination of lattice diffusion and grain boundary diffusion of reactant species through the WC film and slightly grain growth of the WC film.

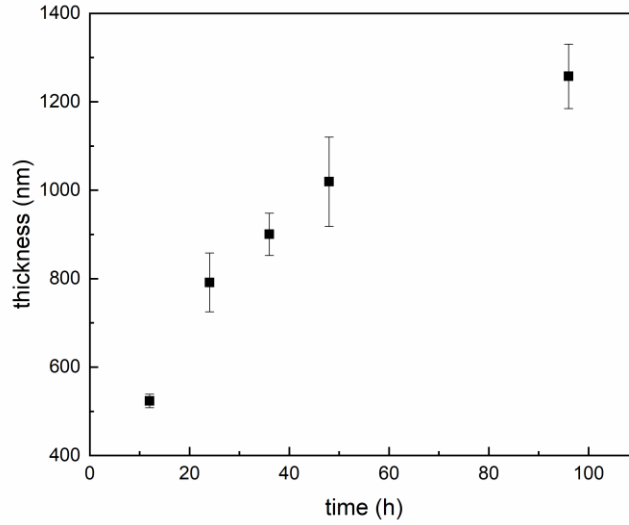


Figure 33. Plot of the WC film thickness versus reaction time for W plates after reaction with pure CO gas at 1000 °C for 12 to 96 h.

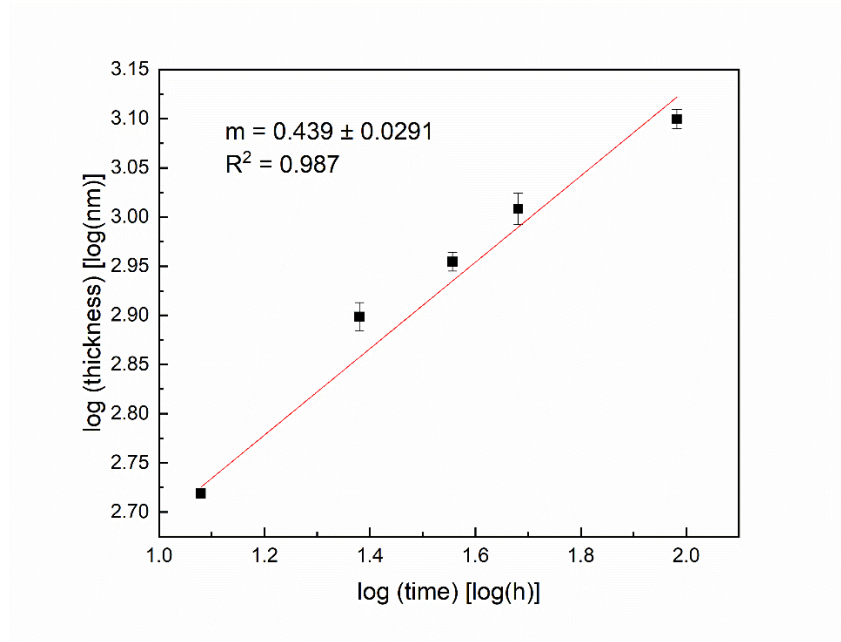


Figure 34. Plot of the log (WC film thickness) versus log (reaction time) for W plates after reaction with pure CO gas at 1000 °C for 12 to 96 h.

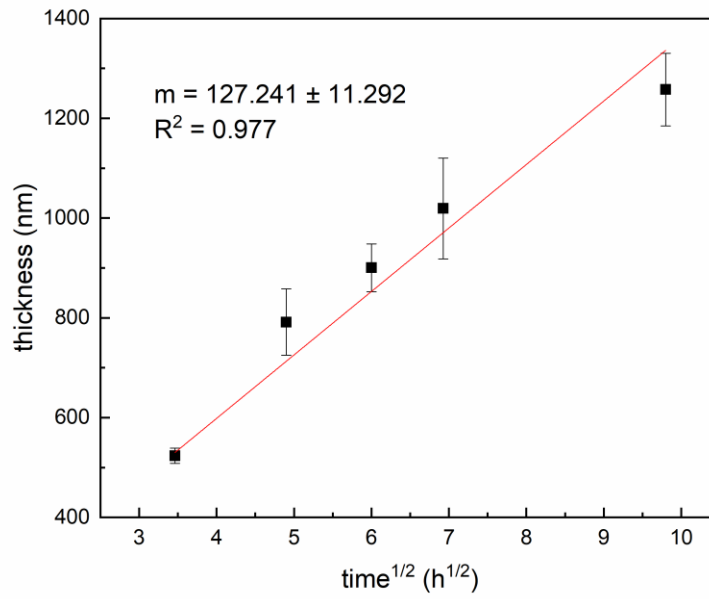


Figure 35. Plot of the WC film thickness versus reaction time^{1/2} for W plates after reaction with pure CO gas at 1000 °C for 12 to 96 h.

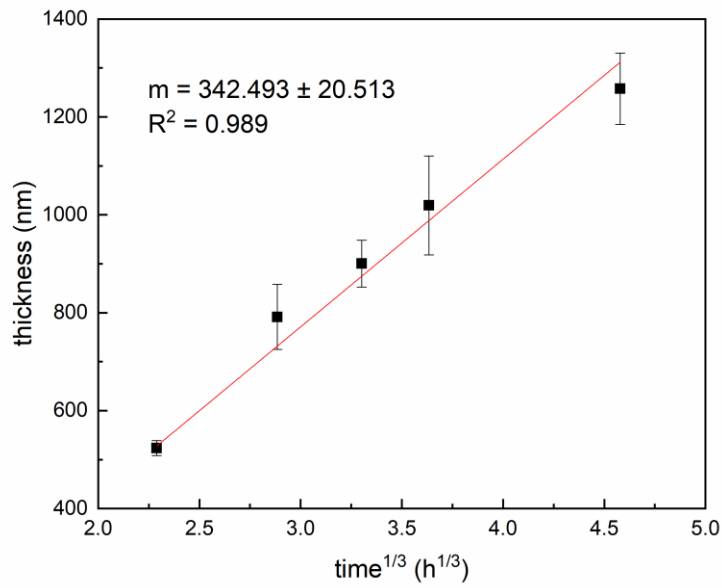


Figure 36. Plot of the WC film thickness versus time^{1/3} for W plates after reaction with pure CO gas at 1000 °C for 12 to 96 h.

The grain size of the WC film for each reaction time was evaluated by calculating the average crystallite size of the WC film from XRD spectrum in Figure 20 via the Williamson-Hall analysis [35]. Williamson-Hall analysis can be described by the following equation:

$$\beta_T = \frac{K\lambda}{D\cos\theta} + 4\varepsilon \frac{\sin\theta}{\cos\theta} \quad (\text{E9})$$

where D is the average crystallite size, K is the shape factor (0.9), λ is the wavelength of the incident beam of XRD analyses (1.5406 Å), ε is the strain between crystallites, and β_T is the peak width (full width at half maximum, FWHM) at a given θ value on the XRD spectrum. The equation can be further rewritten to:

$$\beta_T \cos\theta = \frac{K\lambda}{D} + 4\varepsilon \sin\theta \quad (\text{E10})$$

The Eq. (E10) represents a linear relation between $\beta_T \cos\theta$ and $4\varepsilon \sin\theta$. By plotting $\beta_T \cos\theta$ versus $4\varepsilon \sin\theta$ with different θ , the intercept of the plot, $\frac{K\lambda}{D}$, could be obtained. Then the average crystallite size D can be calculated from the intercept value. The calculated average crystallite sizes for the WC film at each reaction time were summarized in Table 8. A significant growth of WC crystallite with reaction time was not found. Hence, the W carburization with CO gas cannot be completed controlled by the grain boundary diffusion of reactant species through the WC film and grain growth of the WC film. Instead, the reaction is controlled by the combination of lattice diffusion and grain boundary diffusion of reactant species through the WC film and slightly grain growth of the WC film.

Table 8. Calculated crystallite size of the WC film using Williamson-Hall analysis for W plates reacted with pure CO gas at 1000 °C for 12 to 96 h.

Time (h)	Crystallite Size (nm)
12	32
24	41
36	31
48	36
96	36

TEM images of the tungsten plate reacted with CO at 1000 °C for 12 h and 96 h are shown in Figure 37 and Figure 38. Obvious grain growth was not found for a longer carburization time, which was consistent with calculation results from Williamson-Hall analysis. Therefore, the W carburization with CO gas is controlled by lattice diffusion of reactant species through the WC

film, and follows the parabolic rate law. The k values shown in Eq. (E2) for the present work were determined from slopes of the best linear fit line in Figure 25 and Figure 35 as $1.00 \times 10^{-14} \text{ cm}^2/\text{sec}$ and $2.24 \times 10^{-14} \text{ cm}^2/\text{sec}$, respectively. McCarty et al. [36] had studied the tungsten carburization with carbon blacks (under the flow of hydrogen) from 1056 to 1833 °C. The WC formation followed the parabolic rate law, and the activation energy is 58 kcal/mol. The parabolic rate constant k at 1000 °C could be estimated to be $2.58 \times 10^{-14} \text{ cm}^2/\text{sec}$ using the activation energy data for the reaction, which showed a reasonable agreement with the k values obtained in this experiment.

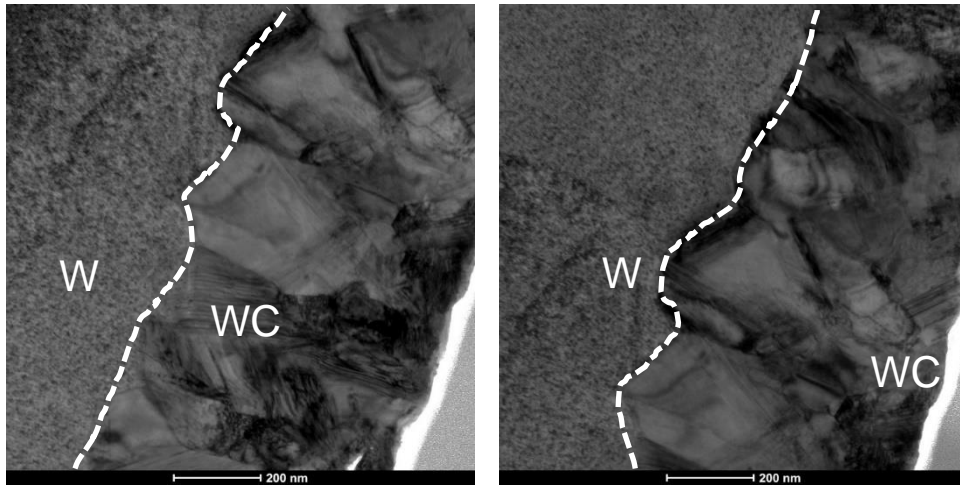


Figure 37. TEM images of the tungsten plate reacted with pure CO gas at 1000 °C for 12 h.

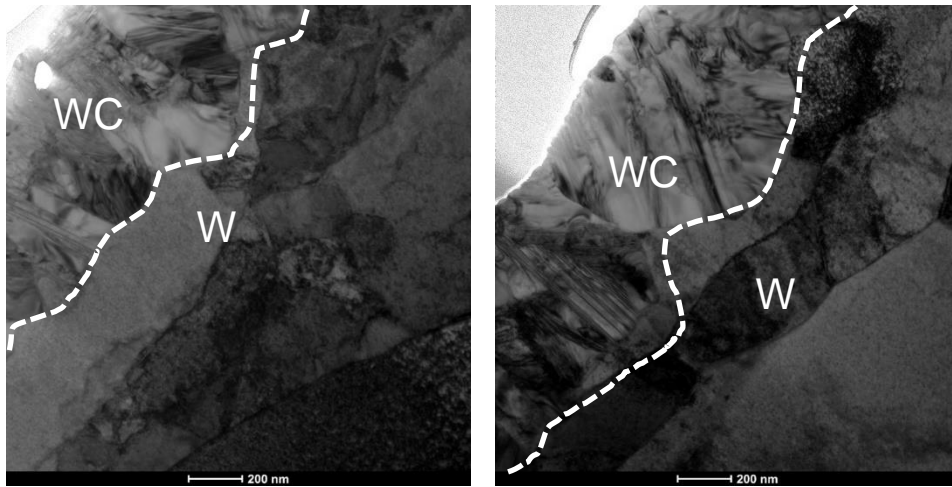


Figure 38. TEM images of the tungsten plate reacted with pure CO gas at 1000 °C for 96 h.

For the inert marker experiment, a SE image and associated EDX elemental maps (for tungsten, magnesium, and oxygen) of the tungsten plate prepared with MgO particles as inert markers before the reaction are shown in Figure 39. MgO particles are sparsely distributed on the surface of the tungsten plate. After the reaction with CO gas at 1000 °C for 96 h, an SE image and associated elemental maps for the carbon, magnesium, oxygen, and tungsten of the same tungsten plate are shown in Figure 40. An SE image from the FIB-cut cross-section of the reacted tungsten plate and associated EDX elemental maps for platinum, magnesium, oxygen, carbon, and tungsten are shown in Figure 41. Platinum was deposited during the FIB-cutting to protect the WC layer on the surface. Figure 40 and Figure 41 indicated that inert markers (MgO particles) only existed on the surface of the reaction-formed WC film. No MgO particles were found within the WC film or at the interface between the WC film and W, which indicated that the formation of the WC film occurred predominately at the WC/W interface. These observations also indicated that the inward diffusion of the C through the WC film was the rate-limiting step for W carburization with CO gas.

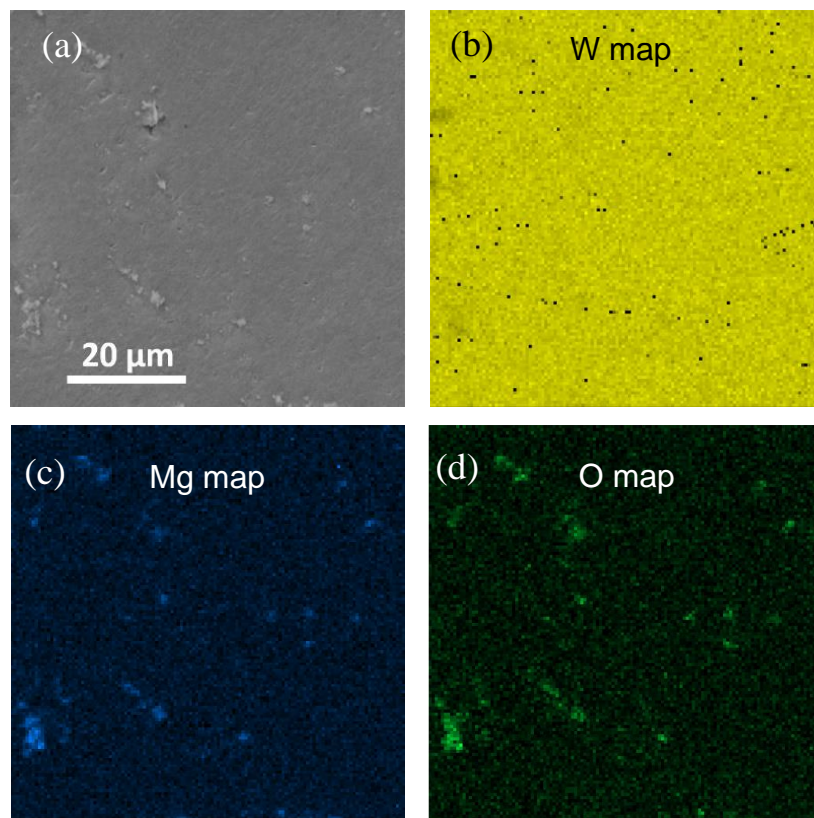


Figure 39. (a) SE image of the large face of the tungsten plate containing MgO particles (inert markers) before the reaction. EDX elemental maps of (b) tungsten, (c) magnesium, and (d) oxygen.

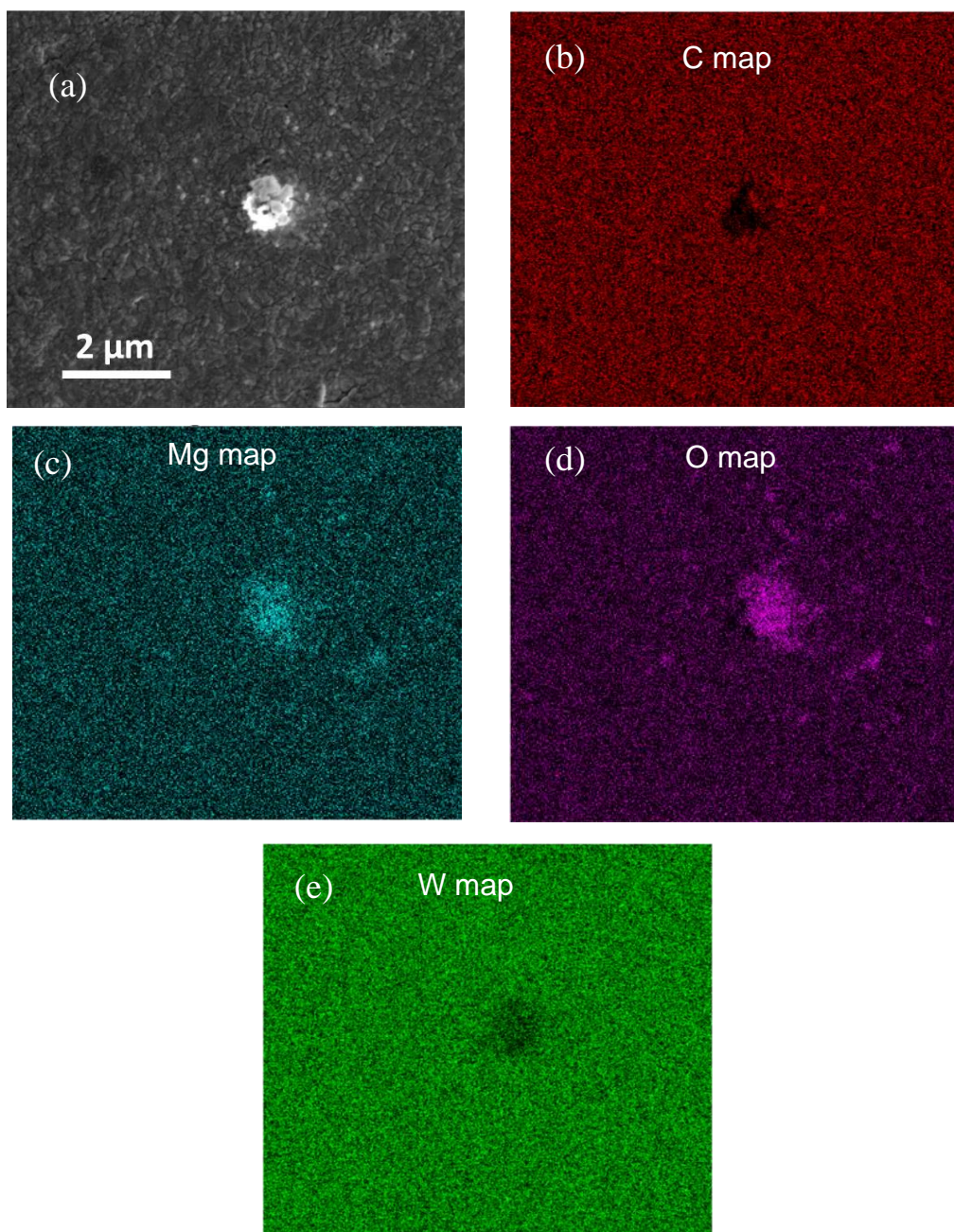


Figure 40. (a) SE image of the large face of the W plate containing MgO particles (inert markers) after the reaction with CO gas at 1000 °C for 96 h. EDX elemental maps of (b) carbon, (c) magnesium, (d) oxygen, and (e) tungsten.

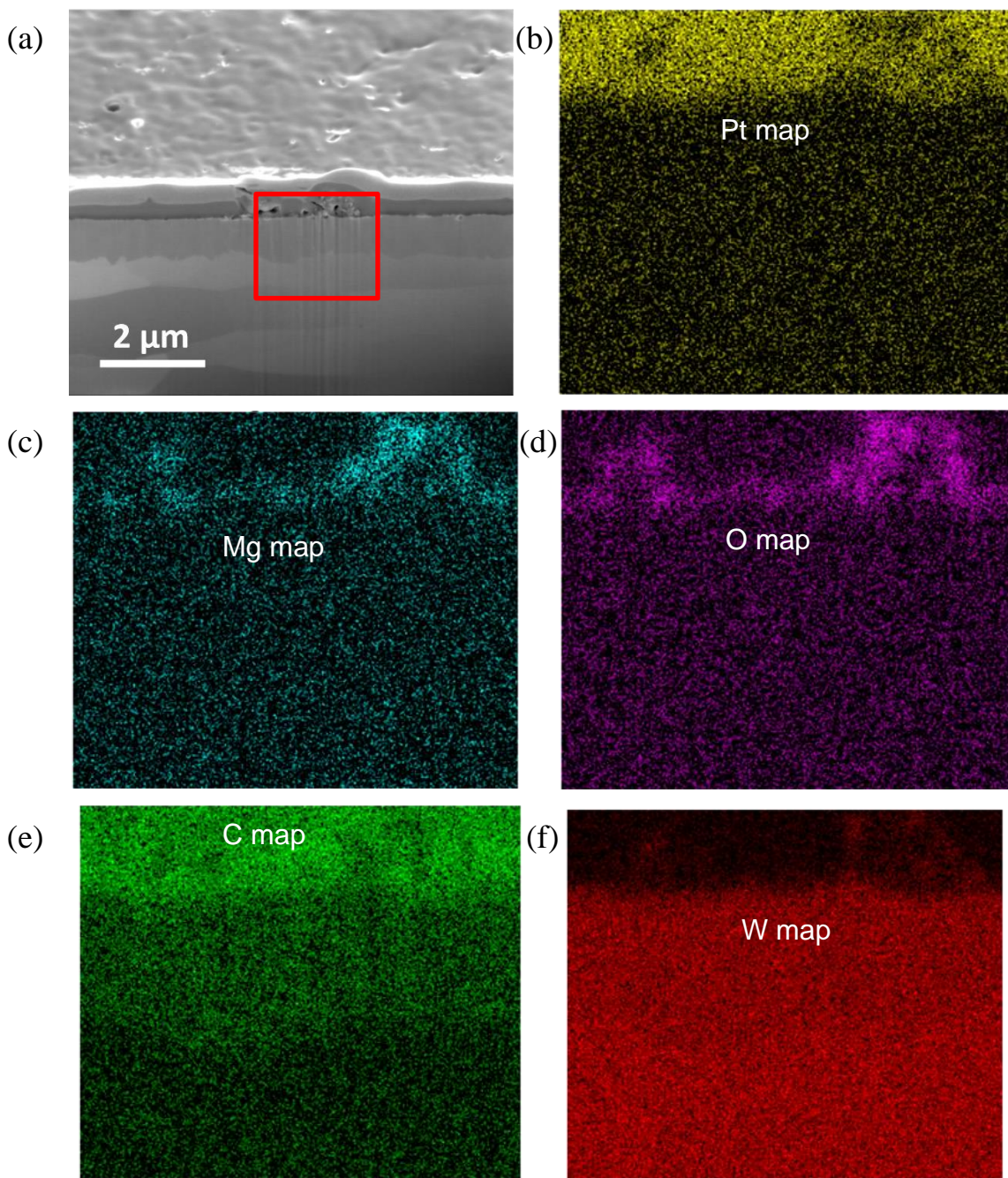


Figure 41. (a) SE image and EDX elemental maps of (b) platinum, (c) magnesium, (d) oxygen, (e) carbon, and (f) tungsten obtained from the FIB-cut cross-section of the tungsten plate containing MgO particles (inert markers) after reaction with CO gas at 1000 °C for 96 h.

4.2 Fabrication of Anisotropic ZrC/W Composites

In order to prove the feasibility of fabricating an anisotropic ZrC/W composite fabricated via the DCP method, W wires were manually wound on a MgO plate. Figure 10b shows the image of the tungsten wires wound on a MgO plate and Figure 42 shows the image of the sintered W wire preform. After sintering, the W wire preform became rigid and could be removed from the MgO plate easily. BSE images from the tilted cross-section and side of the sample are shown in Figure 43. The images in Figure 43 reveal a highly directional structure, and the tilted cross-sectional image shows the connection between wires and available pores for further infiltration. XRD patterns obtained from the surface of the sintered and carburized W wire sample are provided in Figure 44 and Figure 45, respectively. Only peaks associated with W were detected for the sintered sample. For the carburized sample, peaks associated with a WC film were also detected. Therefore, part of the W wire sample was successfully carburized to provide the WC needed to react with Zr_2Cu liquid during the DCP process.

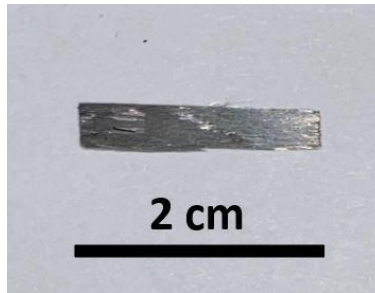


Figure 42. Photograph of the sectioned rectangular W wire preform after sintering at 1800 °C for 2 h with flowing of ultra-high purity argon (99.999%).

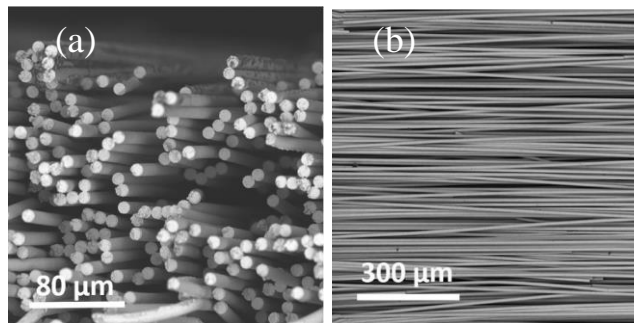


Figure 43. SEM images of the W wire preform sintered at 1800 °C for 2 h with flowing ultra-high purity argon (99.999%) from (a) tilted cross-sectional view and (b) side view.

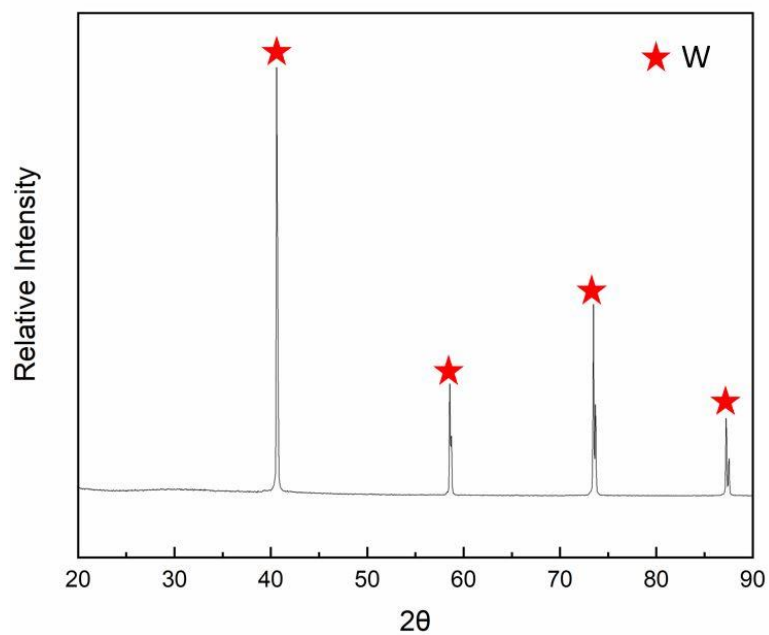


Figure 44. XRD pattern obtained from the surface of the W wire preform sintered at 1800 °C for 2 h with flowing of ultra-high purity argon (99.999%).

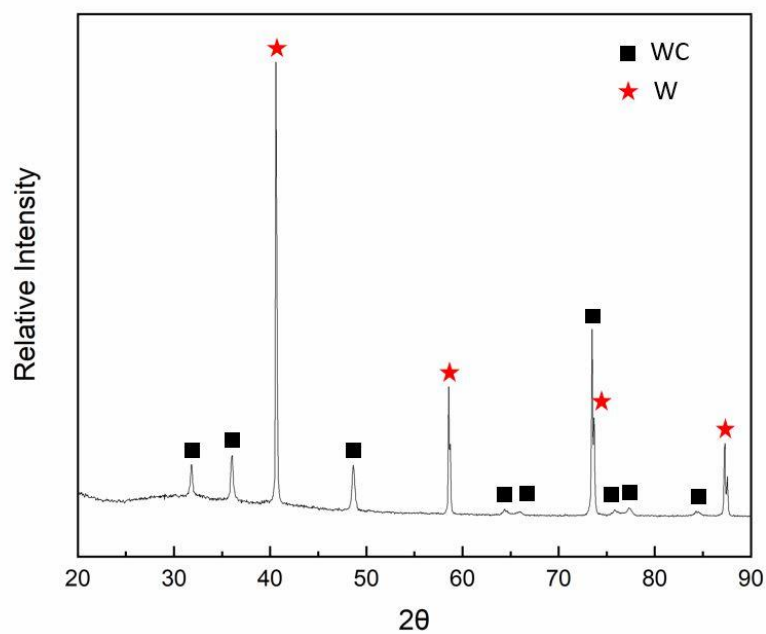


Figure 45. XRD pattern obtained from the surface of the W wire preform after reaction with pure CO gas at 1000 °C for 96 h.

A carburized W wire preform was reactively infiltrated with Zr₂Cu liquid. According to Rxn. (R1), WC reacted with Zr₂Cu (l) to form ZrC. An XRD pattern from the surface of the reacted sample is provided in Figure 46. Peaks associated with W, ZrC, Cu, W₂C, CuO, and ZrO₂ were detected. The sample was successfully infiltrated with Zr₂Cu and formed ZrC/W composites according to the XRD pattern. The possible explanation for W₂C peaks was further C diffusion at high temperatures. Since the DCP process for ZrC/W fabrication requires 1350 °C for the reaction between WC and Zr, carbon from the WC film continued diffusing into the W and formed W₂C. A possible reaction is shown in Rxn. (R5). Further work is needed in the future to confirm the formation mechanism of W₂C.



BSE images and associated elemental maps for oxygen, zirconium, tungsten, and carbon of the infiltrated W wire sample from the cross-section view and side view are shown in Figure 47 and Figure 48, respectively. Bright phases in Figure 47b and Figure 48b indicate that the composite still preserved a high anisotropy. In addition, these bright phases are associated with the tungsten map, which was consistent with W peaks detected by XRD analyses. However, W₂C and W cannot be differentiated from high magnification BSE images as shown in Figure 47a and Figure 48b. TEM analyses are needed on these bright phases to determine where the W₂C is located. Combining with the zirconium and carbon maps, dark phases in BSE images shown in Figure 47 and Figure 48 can be determined as ZrC. Residual Cu from the Zr₂Cu melt was detected by EDX analyses. Oxygen was also detected from the surface, which was consistent with the detection of CuO and ZrO₂ peaks from the XRD analyses. In summary, the XRD analyses and EDX analyses indicate that the sample was successfully converted to a ZrC/W composite with highly anisotropic W and W₂C phases. The method for fabricating anisotropic ZrC/W via the DCP process using tungsten wires for preform preparation is feasible.

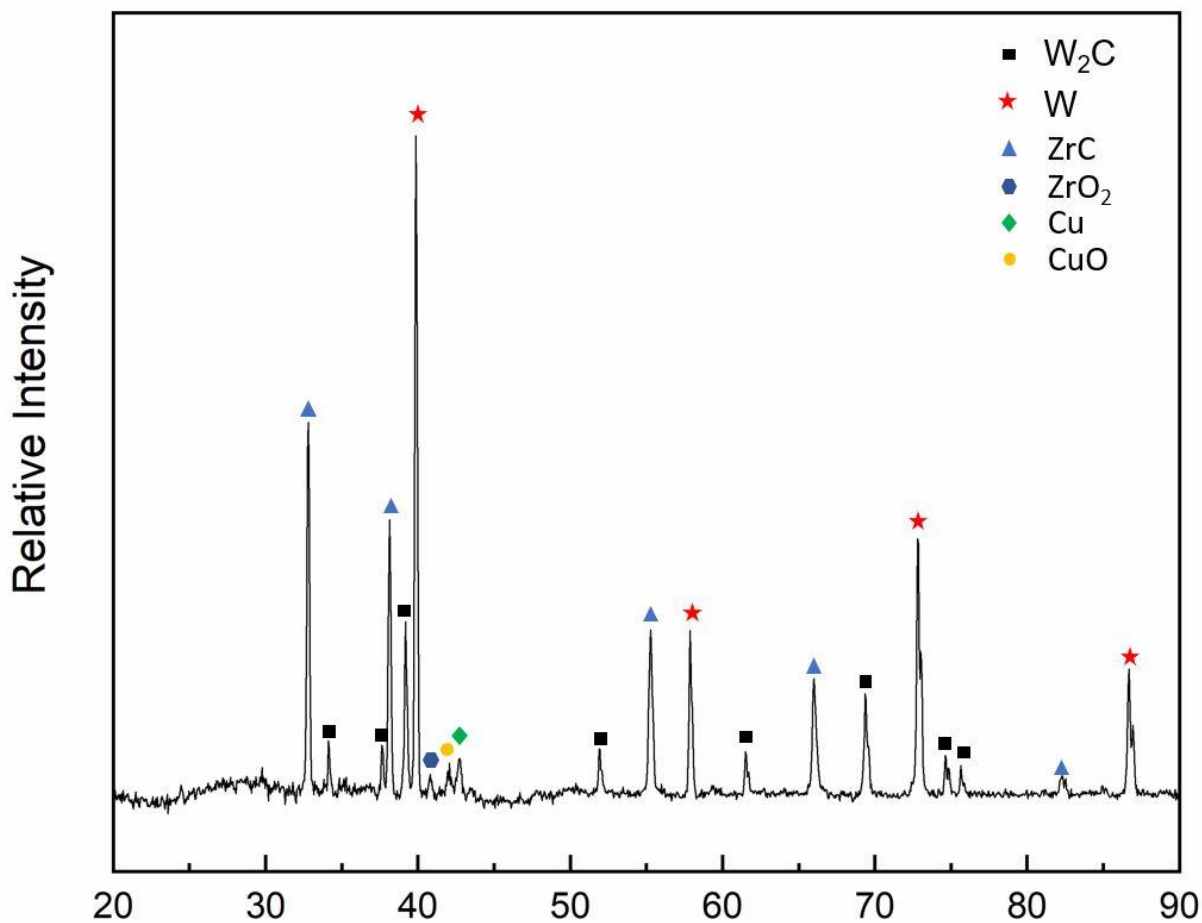


Figure 46. XRD pattern obtained from the surface of the W wire sample reactively infiltrated with Zr_2Cu at 1350 °C.

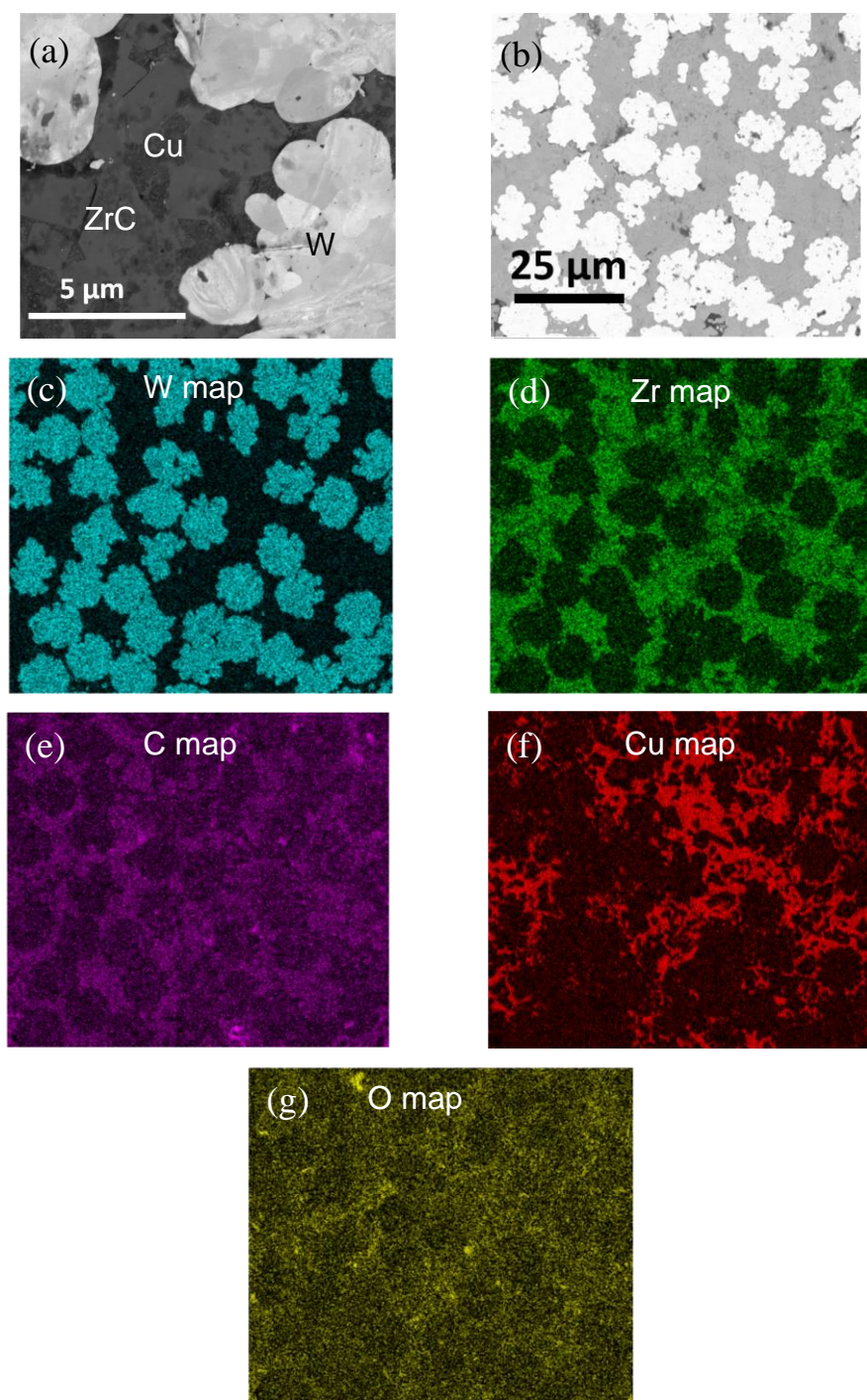


Figure 47. BSE images from a cross-sectional view of the reactive infiltrated carburized W wire preform at (a) a high magnification and (b) a lower magnification and associated elemental maps of (c) tungsten, (d) zirconium, (e) carbon, (f) copper, and (g) oxygen.

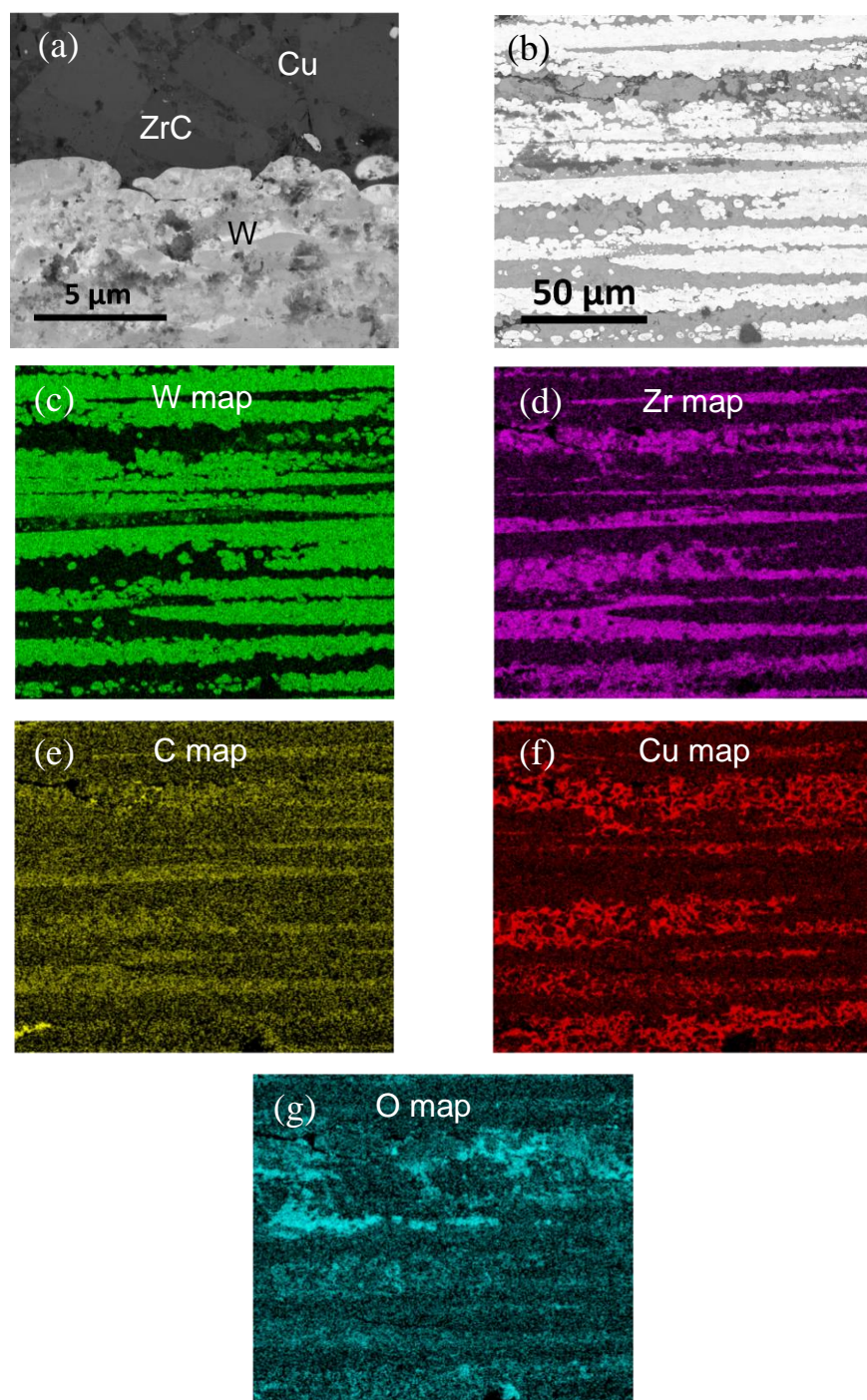


Figure 48. BSE images from a side view of the reactive infiltrated carburized W wire preform at (a) a high magnification and (b) a lower magnification and associated elemental maps of (c) tungsten, (d) zirconium, (e) carbon, (f) copper, and (g) oxygen.

5. CONCLUSIONS

Dense and continuous WC films were successfully formed by carburizing the W plates by reaction with CO gas at 1000 °C. W plates were heated to 1000 °C in argon atmosphere, and then reacted with CO gas for 12 h to 96 h. EDX, XRD, and SAED analyses confirmed the phase content of the formed layer as only WC. Mass change data for each sample was directly measured with an electronic balance. The WC film thicknesses were evaluated by direct measurement from FIB-cut cross-sections. Both mass change per unit area data and thickness change data have better linear fittings to the 1/3 of reaction time, which indicates a cubic rate law for the W carburization with CO gas. But logarithm plots of mass change per unit area and thickness change versus reaction preserve slopes between 1/2 and 1/3. In addition, no significant grain growth was found for WC film with different reaction times. Hence, the W carburization with CO gas at 1000 °C was controlled by the lattice diffusion through the WC film and follows the parabolic rate law. The parabolic rate constants k were determined as $1.00 \times 10^{-14} \text{ cm}^2/\text{sec}$ and $2.24 \times 10^{-14} \text{ cm}^2/\text{sec}$ from the weight change data and the thickness change data. The obtained k values showed a reasonable agreement with the k value for the W carburization with carbon blacks at 1000 °C. From the inert marker experiment, MgO particles (inert markers) were only found on the external surface of the WC film, which indicated that the formation of the WC film occurred predominately at the WC/W interface and that inward diffusion of C through the WC film was the rate-limiting step.

Tungsten wire preforms were fabricated by hand-winding and sintering at 1800 °C for 2 h. The rigid preforms were carburized with CO gas at 1000 °C for 96 h. XRD analyses confirmed the formation of WC. A carburized preform was then successfully converted into an anisotropic ZrC/W-bearing composite via the DCP method by reaction with the Zr_2Cu melt. The ZrC/W-bearing composite preserved a high anisotropy of the W wire preform. XRD and EDX analyses confirmed the conversion of WC to W and ZrC. W_2C was found from XRD analyses but not from the observation from SEM images. W_2C may be formed due to the further reaction between WC and C. Future work is needed to confirm the kinetic mechanism of the W_2C formation.

REFERENCES

- [1] Evans, A.G. and Marshall D.B. The mechanical behavior of ceramic matrix composites. *Acta Metall.*, 37(10), 2567-2583 (1989).
- [2] Chawla, N. and Shen. Y. Mechanical behavior of particle reinforced metal matrix composites. *Adv. Eng. Mat.*, 3(6), 357-370 (2001).
- [3] Speyer, F. Ablative composites containing in situ reaction-formed refractory metal carbides. *Ind. Eng. Chem. Prod. Res. Develop.*, 10(1), 99-111 (1971).
- [4] Raddatz, O., Schneider, G.A., Mackens, W., Voss, H. and Claussen, N. Bridging stresses and R-curves in ceramic/metal composites. *J. Euro. Ceram. Soc.*, 20(13), 2261-2273 (2000).
- [5] Eremenko, V. N., Velikanova, T. Y., Artyukh, L. V., Aksel'rod, G. M. & Vishnevskii, A. S. In *Phase Equilibria Diagrams. Phase Diagrams for Ceramists*. Vol. X. (ed. A. E. McHale) Fig. 9034 (The American Ceramic Society, Westerville, OH, USA, 1994).
- [6] Storms, E.K.R., *The Refractory Carbides*. (Academic Press, New York, NY, 1967) p. 18.
- [7] Lassner E, Schubert W-D. *Tungsten—properties, chemistry, technology of the element, alloys and chemical compounds*. Springer-Verlag; (1999).
- [8] Dickerson, M. B., Wurm, P. J., Schorr, J. R., Hoffman, W. P. & Sandhage, K. H., Near net-shaped, ultra-high melting, recession-resistant ZrC/W-based rocket nozzle liners via the displacive compensation of porosity (DCP) method. *J. Mater. Sci.* 39, 6005-6015 (2004).

- [9] Caccia, M., Tabandeh-Khorshid, M., Itskos, G., Strayer, A. R., Caldwell, A. S., Pidaparti, S., Singnisai, S., Rohskopf, A. D., Schroeder, A. M., Jarrahbashi, D., Kang, T., Sahoo, S., Kadasala N. R., Marquez-Rossy, A., Anderson, M. H., Lara-Curzio, E., Ranjan, D., Henry, A. & Sandhage, K. H. Ceramic–metal composites for heat exchangers in concentrated solar power plants. *Nature*. 562(7727), 406–409 (2018).
- [10] Song, G.M., Wang, Y.J. & Zhou Y., The mechanical and thermophysical properties of ZrC/W composites at elevated temperatures. *Mater Sci Eng A*, A334, pp. 223-232 (2002).
- [11] Kumar, P. & Sandhage K. H., US Patent Application no. 60/083, 534 (April 29.1998)
- [12] Kumar, P. & Sandhage K. H., Method for Fabricating Shaped Monolithic Ceramics and Ceramic Composites Through Displacive Compensation of Porosity, and Ceramics and Composites made Thereby, U.S. Patent No. 6,407,022 (June 18, 2002).
- [13] Song, G. M., Wang, Y. J. & Zhou, Y., The mechanical and thermophysical properties of ZrC/W composites at elevated temperature. *Materials Science and Engineering A*, 334(1–2), 223–232 (2002).
- [14] Zhang, K., Shi, Z., Xia, H., Wang, K., Liu, G., Qiao, G. & Yang, J., Preparation and thermophysical properties of directional SiC/Cu–Si composite via spontaneous infiltration. *Ceramics International*, 42(1), 996–1001 (2016).
- [15] Roy, S., Albrecht, P., Przybilla, L., Weidenmann, K. A., Heilmaier, M. & Wanner, A., Effect of Phase Architecture on the Thermal Expansion Behavior of Interpenetrating Metal/Ceramic Composites. *Processing and Properties of Advanced Ceramics and Composites V*, 240, 33–44., (2013).
- [16] Lawn, B., *Fracture of Brittle Solids*, 2nd ed. Cambridge University Press, 1993, p. 210.

- [17] Lipke, D. W., Novel reaction processing techniques for the fabrication of ultra-high temperature metal/ceramic composites with tailorable microstructures. [Doctoral dissertation, Georgia Institute of Technology]. *SMARTech* (2013).
- [18] Alexander, B. H. & Balluffi, R. W., The mechanism of sintering of copper. *Acta Met.*, vol. 5, no. 11, pp. 666–677 (1957).
- [19] Ives, R. L., Member, S., Falce, L. R., Schwartzkopf, S. & Witherspoon, R., Controlled Porosity Cathodes from Sintered Tungsten Wires. *IEEE TRANSACTIONS ON ELECTRON DEVICES*, 52(12), 2800–2805 (2005).
- [20] Schwartzkopf, P. & Kiffer, R., *Refractory Hard Metals & Borides, Carbides, Nitrides, and Silicides*. The MacMillan Company, New York (1953).
- [21] Lemaitre, J., Benoit, V. & Delmon, B., Control of the Catalytic Activity of Tungsten Carbides. *Journal of Catalysis*, 99, 415–427 (1986).
- [22] Hojo, J., Shimogama T. & Kato, A., Carburization Rates of Molybdenum and Tungsten with Methane. *NIPPON KAGAKU KAISHI*, vol. 9, 1174–1180 (1979).
- [23] Giraudon, J. M., Devassine, P., Lamonier, J. F., Delannoy, L., Leclercq, L. & Leclercq, G., Synthesis of tungsten carbides by temperature-programmed reaction with CH₄-H₂ mixtures. Influence of the CH₄ and hydrogen content in the carburizing mixture. *Journal of Solid State Chemistry*, 154(2), 412–426, (2002).
- [24] Fang, X., Kreter, A., Rasinski, M., Kirchlechner, C., Brinckmann, S., Linsmeier, C. & Dehm, G., Hydrogen embrittlement of tungsten induced by deuterium plasma: *Insights from nanoindentation tests*. *Journal of Materials Research*, 33(20) (2018).
- [25] Tedmon, C., The effect of oxide volatilization on the oxidation kinetics of Cr and Fe-Cr alloys. *Journal of the Electrochemical Society*, vol. 113, no. 8, pp. 766-768 (1966).

- [26] Levenspiel, Octave. *Chemical reaction engineering. Industrial & engineering chemistry research*. 38.11 (1999): 4140-4143.
- [27] Suryanarayana, D., Oxidation kinetics of aluminum nitride. *Journal of the American Ceramic Society*, vol. 73, no. 4, pp. 1108-1110 (1990).
- [28] Tammann, G., Über Anlauffarben von metallen. *Zeitschrift für anorganische und allgemeine Chemie*, vol. 111, no. 1, pp. 78-89 (1920).
- [29] Bedworth, R. & Pilling, N., The oxidation of metals at high temperatures. *J Inst Met*, vol. 29, no. 3, pp. 529-582 (1923).
- [30] Wagner, C., Beitrag zur theorie des anlaufvorgangs. *Zeitschrift für physikalische Chemie*, vol. 21, no. 1, pp. 25-41 (1933).
- [31] Perrow, J. M., Smeltzer, W. W. & Embury, J. D., The role of structural defects in the growth of nickel oxide films. *Acta Metallurgica*, 16.10 (1968): 1209-1218.
- [32] Joint Committee on Powder Diffraction Standards (JCPDS) International Center for Diffraction Data (2018) File 00–051–0939 for WC. <http://www.icdd.com/index.php/pdf-4> (JCPDS International Center for Diffraction Data, Newtown Square).
- [33] Joint Committee on Powder Diffraction Standards (JCPDS) International Center for Diffraction Data (2018) File 00-004-0806 for W. <http://www.icdd.com/index.php/pdf-4> (JCPDS International Center for Diffraction Data, Newtown Square).
- [34] Barin, I., *Thermochemical Data of Pure Substances 3rd edn*. 1995, Wiley, Hoboken, NJ, USA.
- [35] Williamson, G. K. & Hall, W. H., X-ray line broadening from filed aluminium and wolfram. *Acta Metallurgica*, Vol. 1, pp. 22–31 (1953).

- [36] McCarty, L. V., Donelson, R. & Hehemann, R. F., A diffusion model for tungsten powder carburization. *Metallurgical Transactions. A*, Physical Metallurgy and Materials Science, 18 A(6), 969–974 (1987).